

# Fully passive siphon-driven salt removal surpassing diffusion limits in solar distillation

Roberto Raffaele Meo <sup>a</sup>, Stefan Morosanu <sup>a</sup>, Matteo Morciano <sup>a,b</sup>,\* , Matteo Fasano <sup>a,b</sup>

<sup>a</sup> Department of Energy, Politecnico di Torino, Corso Duca degli Abruzzi 24, 10129 Torino, Italy

<sup>b</sup> Clean Water Center, Politecnico di Torino, Corso Duca degli Abruzzi 24, 10129 Torino, Italy

## HIGHLIGHTS

- Fully passive siphon removes salt from porous solar evaporators autonomously.
- Evaporation-driven hydraulic head triggers self-sustained rinsing cycles.
- Validated analytical model predicts hydraulic head and rinsing frequency.
- Evaporator salinity restored to seawater levels within 3 h.
- Salt removal >10× faster than diffusion-limited passive methods.

## ARTICLE INFO

Dataset link: <https://doi.org/10.5281/zenodo.17422758>

### Keywords:

Passive desalination  
Siphon mechanism  
Salt removal  
Solar energy  
Sustainable distillation

## ABSTRACT

Salt accumulation is a key bottleneck in solar- and waste-heat driven passive distillation systems, where evaporation inevitably leads to salt buildup that compromises long-term performance. Here, the first evaporation-driven siphon architecture enabling fully passive and autonomous salt removal from a porous evaporator is introduced. The device operates in a fully passive manner, relying solely on evaporation-induced hydraulic head differences. The system functions without external energy, active control, or moving parts. An analytical model, developed through the electric-hydraulic analogy, predicts both the transient evolution of evaporation-induced hydraulic head difference and the frequency of self-triggered rinsing cycles, and is validated experimentally under controlled conditions. A case study shows that the system generates hydraulic head differences exceeding 1.5 cm and triggers multiple rinsing events within hours. Parametric analysis reveals that geometry and hydraulic resistance of the porous evaporator strongly influence performance, and that a simple topological modification – introducing a localized high-resistance segment – further boosts hydraulic head buildup. Compared to state-of-the-art passive strategies limited by diffusion, the siphon-driven mechanism achieves over an order-of-magnitude faster salt removal, restoring seawater-level salinity within three hours. These results establish a new paradigm in solar distillation, providing a scalable strategy compatible with meter-scale evaporators and capable of drastically reducing maintenance requirements for robust salt management in evaporation-driven applications, e.g. desalination, particularly suited to off-grid and resource-limited environments.

## 1. Introduction

The growing scarcity of freshwater represents a critical global challenge, with profound environmental, economic, and social consequences (Kelley et al., 2015; Mekonnen and Hoekstra, 2016; Stincone et al., 2024). Contributing factors such as climate change, overexploitation of natural water resources, and population growth have worsened this crisis. Projections indicate that global water consumption is expected to grow 55% by 2050 (World Water Assessment Programme, 2016; Meo et al., 2025), with more than 40% of the world's population

living in regions facing severe water shortages. Currently, approximately 768 million people lack access to safe drinking water (World Water Assessment Programme, 2016; Meo et al., 2025). The impact is particularly severe in areas where financial constraints limit the adoption of expensive water production technologies that rely on conventional power grids (Mauter and Fiske, 2020; Angelis et al., 2021; Stincone et al., 2024). As a result, the development of sustainable and affordable solutions is crucial for addressing this crisis and ensuring access to water resources for future generations.

\* Corresponding author at: Department of Energy, Politecnico di Torino, Corso Duca degli Abruzzi 24, 10129 Torino, Italy.  
E-mail address: [matteo.morciano@polito.it](mailto:matteo.morciano@polito.it) (M. Morciano).

<https://doi.org/10.1016/j.jclepro.2026.148137>

Received 21 November 2025; Received in revised form 6 March 2026; Accepted 25 March 2026

Available online 30 March 2026

0959-6526/© 2026 The Authors. Published by Elsevier Ltd. This is an open access article under the CC BY license (<http://creativecommons.org/licenses/by/4.0/>).

Seawater desalination has emerged as a key solution to the escalating water crisis (Kumar et al., 2022; Meo et al., 2025). However, conventional desalination methods are heavily reliant on fossil fuels, resulting in high energy costs and contributing to environmental concerns such as carbon emissions (He et al., 2023; Sharon and Reddy, 2015; Meo et al., 2025).

In response, research has increasingly focused on the development of sustainable, energy-efficient, and passive desalination technologies (Meo et al., 2023, 2025). Among these, solar- or waste-heat driven passive distillation has gained prominence due to its ability to function without mechanical components, making it particularly suitable for remote and off-grid locations (Zhang et al., 2020; Chiavazzo et al., 2018; Stincone et al., 2024). Recent advances in the field have explored techniques to optimize performance (Stincone et al., 2024). Several approaches have been investigated, including the incorporation of carbon-based absorbers (Liu et al., 2017; Li et al., 2018; Yang et al., 2018). Other studies have focused on nanomaterials (Wang et al., 2017; Mauter et al., 2018; Wang et al., 2018). Polymers have also been explored as functional materials (Li et al., 2019; Huang et al., 2017). Despite these advancements, a persistent challenge in solar-driven evaporation systems is managing salt accumulation, which can significantly degrade long-term efficiency and scalability (Kuang et al., 2019; Zhang et al., 2019; Stincone et al., 2024).

Several strategies have been explored to address this issue, leveraging mechanisms such as ionic backflow, engineered surface treatments, and asymmetric membrane designs (Xu et al., 2021). However, each approach presents limitations in terms of durability, scalability, or operational complexity. Passive strategies based on ionic backflow enable partial self-cleaning by redissolving salt and promoting its diffusion back into the bulk. For example, Zhang et al. (2024) demonstrated a 3D melamine sponge-polypyrrole evaporator with high evaporation rates and temporary mitigation of salt buildup through edge-priority crystallization and nocturnal back-diffusion. Yet, the efficiency of this process is strongly dependent on diurnal cycling (distillation during the day; salt removal during the night) and salinity conditions. Salt-washable surface designs, such as the GRAMS (Graphene-Recycled Au-Melamine Sponge) device (Li et al., 2024), improve maintainability by facilitating salt removal via gravity or simple rinsing. While promising in terms of regeneration and portability, these systems often require manual intervention or periodic downtime to maintain performance. Architected devices with controlled salt deposition zones (e.g., nitrocellulose-based evaporators (Yang et al., 2023)) enable localized salt harvesting without compromising evaporation in central regions. However, the fine-tuning required for such designs can limit their adaptability to variable environmental and feedwater conditions. Janus membranes with asymmetric wettability, such as vertically aligned MXene aerogels (Zhang et al., 2019), can effectively inhibit salt accumulation through directional water transport. While achieving stable performance over extended periods, the fabrication of such advanced materials remains complex, posing challenges for large-scale deployment. Other approaches, such as those leveraging Marangoni-driven fluid dynamics (Lei et al., 2022; Chen et al., 2023; Stincone et al., 2024), have shown potential for improving salt transport and rejection by significantly enhancing solute movement. In particular, the recent study by Stincone et al. (2024) provides a comprehensive numerical investigation on the role of the Marangoni effect in mitigating salt accumulation. Their sensitivity analysis demonstrates that Marangoni-induced mass transport can outperform purely diffusive flow. Notably, their simulations indicate that nighttime brine discharge can rapidly restore seawater-like salinity levels within two hours, setting a new benchmark in the field. However, further theoretical and experimental work is needed to scale up these strategies.

Given the ongoing challenges of current passive desalination methods, innovative solutions are being explored to enhance efficiency and scalability. One such solution is siphon-based salt rejection, which offers a novel approach while maintaining simplicity and adaptability.

Siphon-based systems have recently gained attention as a promising means of addressing salt accumulation in passive solar distillation and desalination. Xue et al. (2024) developed a siphon-assisted evaporator with a  $\text{Co}_3\text{O}_4$  nanoneedle array on a graphene-based solar absorber, successfully preventing salt accumulation even at high salinities. Similarly, Fan et al. (2023) introduced a spatial evaporation device incorporating a hydrogel-based evaporator and 3D-printed module, demonstrating the effectiveness of siphon-driven fluid circulation. Deka et al. (2025) expanded on this by demonstrating the scalability of siphon systems in multistage thermal desalination setups, showcasing their potential for large-scale applications. However, existing siphon-based distillation/desalination systems still require an externally imposed hydraulic head difference to trigger and sustain siphoning, relying on manual intervention or auxiliary energy input. This dependence prevents fully passive operation.

The novelty of the present work does not lie in the siphon concept itself, which has been previously explored, but in demonstrating that the siphon activation head can be generated autonomously during operation in a fully passive way, in order to achieve autonomous salt removal from the porous evaporator. The key innovation is harnessing evaporation-driven mass loss to disrupt hydraulic equilibrium and passively generate the head difference required for siphon activation. The analytical model developed employs the electric-hydraulic analogy to predict the passively induced head differences and frequency of siphon-triggered rinsing cycles. The model forecasts that, after 8 h of solar exposure, hydraulic heads on the order of centimeters to tens of centimeters can be achieved, with the evaporator undergoing over ten rinsing cycles. Experimental validation under controlled conditions confirms the system's ability to induce the predicted hydraulic gradients and fully regenerate the evaporator through self-sustained rinsing cycles. Furthermore, optimization of the evaporator and siphon-inducing device design can significantly improve system performance. It is worth noting that, while Marangoni-driven transport can achieve salt rejection rates comparable to siphon rinsing (Stincone et al., 2024), it requires the presence of a liquid-air interface and has so far been demonstrated only at small scales, with performance strongly dependent on concentration gradients. In contrast, the siphon mechanism operates independently of interfacial effects and gradient strength, offering a more robust and scalable pathway for passive salt management.

Therefore, this study establishes a new paradigm for fully passive distillation by enabling autonomous salt removal at the evaporator level. It is predicted that evaporation-driven siphons autonomously remove salt from the evaporator over extended periods without any external energy input, moving parts, or active control. The approach offers a scalable and maintenance-free solution for distillation, desalination and other evaporation-driven applications, particularly well suited for remote and resource-limited areas.

## 2. Methods

This section presents the methodological framework adopted to analyze the proposed spontaneous salt-disposal device integrated with an evaporation-driven distillation system. First, the device concept and its working principle are introduced. Subsequently, the hydraulic model based on the electric-hydraulic analogy is described, followed by a simplified Thevenin-equivalent formulation and the experimental validation of the proposed approach.

### 2.1. Device concept and working principle

The system depicted in Fig. 1 integrates a spontaneous salt-disposal device with an evaporation-based distillation unit. The distillation unit consists of an inverted U-shaped porous medium with two inlets for saline water uptake. Solar irradiation induces evaporation across the horizontal section of the inverted U-shaped structure.

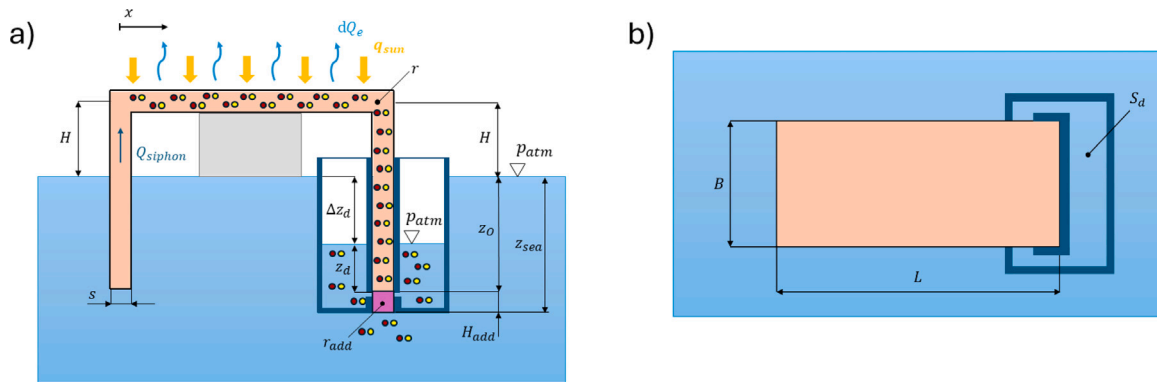


**Fig. 1.** Schematic representation of the spontaneous salt-disposal device integrated with the evaporation-based distillation system. (a) Sectional view of the system, illustrating the inverted U-shaped porous evaporator and the integrated spontaneous salt-disposal device. Impermeable walls/materials delineating the salt-disposal pocket are highlighted in dark blue. The key geometric parameters are indicated: the horizontal evaporator is positioned at height  $H$  above sea level, with porous medium thickness  $s$ , pore radius  $r$ , and an additional resistance characterized by pore radius  $r_{add}$  and a length  $H_{add}$ . The right end of the porous medium is located at a depth  $z_0$ , while the additional resistance is in contact with the sea at  $z_{sea}$ . The water level inside the salt-disposal device reaches  $z_d$ , defining the hydraulic head difference  $\Delta z_d = z_0 - z_d$ . The reference coordinate system  $x$  is also indicated. A narrow slit in the impermeable wall hydraulically connects the pocket to the porous medium. Solar irradiance  $q_{sun}$  induces localized evaporation  $dQ_e$ , concentrating salt molecules (represented by red and yellow circles). Some salt accumulates in the disposal device displaced by siphon-induced flow  $Q_{siphon}$ , while the rest is discharged into the sea. (b) Top view of the system, highlighting the evaporator footprint: width  $B$  and length  $L$ . The salt-disposal device section  $S_d$  is also indicated.

The salt-disposal device, mounted at one of the inlets (the one on the right in Fig. 1a), functions analogously to a piezometer and incorporates an additional high hydraulic resistance with tailored geometry (pore radius  $r_{add}$  and a length  $H_{add}$ , see Fig. 1a) in series with that of the vertical leg of the system. Impermeable walls (highlighted in dark blue in Fig. 1a) delineate the salt-disposal device, creating a pocket and forcing water to flow exclusively through the additional high hydraulic resistance. Evaporation-induced water flow causes a pressure drop across this hydraulic resistance. The static pressure intake of the piezometer is located just upstream of the added hydraulic resistance. During evaporation-driven flow, viscous losses across this resistance reduce the local pressure at the intake compared to the static case. To match this lower pressure, the water level inside the salt-disposal device decreases, resulting in a free surface elevation lower than sea level. The height of the water column inside the device reflects the reduced pressure at the intake, according to Stevin's principle.

When evaporation stops and flow ceases, the pressure returns to equilibrium, and the water level in the device rises again, passively refilling from the sea. Refilling can occur through two paths: via the additional resistance or through the opposite inlet by siphoning. To remove accumulated salt from the evaporator, the system is designed to promote filling by siphon effect, ensuring water flows through the evaporator, rinsing it and transferring salt deposits into the disposal device. Salt removal from such disposal device to the sea can then occur through mechanisms such as diffusion or one-way valves, though these aspects are not detailed at this stage. A particularly interesting scenario arises when the hydraulic resistance at the inlet becomes infinite, i.e. effectively isolating the inlet from the sea and enabling interaction exclusively with the salt disposal device.

## 2.2. Hydraulic model

The electric-hydraulic analogy is used as the foundational framework to model fluid dynamics in the siphon-based salt removal device proposed in this work. This approach allowed us to conceptualize and quantify the viscous losses within the porous medium, which plays a critical role in the capillary water flow driven by solar-induced evaporation.

Viscous losses within the porous medium were modeled through its permeability, estimated via the Kozeny-Carman correlation (Nishiyama

and Yokoyama, 2017). The permeability  $K$  of the porous medium is given by:

$$K = \frac{\epsilon r^2}{\gamma \tau^2}, \quad (1)$$

where  $\epsilon$  is the porosity of the porous medium, defined as the ratio of the void volume to the total volume of the medium,  $r$  is the mean radius of the pores,  $\gamma$  is a parameter that depends on the pore shape and geometry, and  $\tau$  is the tortuosity of the porous medium, which accounts for the discrepancy between the actual mean flow path length and the thickness of the porous medium. For circular pores, as those assumed in this study,  $\gamma = 8$  (Nishiyama and Yokoyama, 2017). The tortuosity  $\tau$  is evaluated using the Mackie-Mearns equation  $\tau = \frac{(2-\epsilon)^2}{\epsilon}$ , which provides a robust means of quantifying how the porosity affects the flow path's complexity and, consequently, the effective transport properties of the medium.

The pressure drop  $\Delta p$  across the porous medium is then given by Meo and Morciano (2022):

$$\Delta p = \frac{\epsilon \mu}{K} L v, \quad (2)$$

where  $\mu$  is the dynamic viscosity,  $L$  is the length of the porous medium, and  $v$  is the flow velocity through the pores. Considering the definition of permeability  $K$  in Eq. (1) and defining the velocity  $v$  as the ratio of the flow rate  $Q$  to the effective cross-sectional area  $\epsilon A$  of the porous medium, the pressure drop becomes:

$$\Delta p = \frac{8 \mu \tau^2}{\epsilon A r^2} L Q. \quad (3)$$

Starting from the hydraulic analogy  $\Delta p = R_{hydr} Q$ , which relates the pressure drop  $\Delta p$  across a flow path to the volumetric flow rate  $Q$  through the hydraulic resistance  $R_{hydr}$ , the hydraulic resistance of the porous medium can be expressed as:

$$R_{hydr} = \frac{8 \mu \tau^2}{\epsilon A r^2} L. \quad (4)$$

The hydraulic resistance  $R_{hydr}$  encapsulates the influence of the porous medium's structural and material properties on the flow resistance, serving as a critical parameter for evaluating the device's efficiency.

As illustrated in Fig. 1, the device comprises three main sections of porous medium: the left vertical section, the right vertical section, and the central horizontal evaporator, each contributing a distinct hydraulic resistance due to its porous structure. Beyond these resistances, the hydraulic model also incorporates elevation effects and fluid storage

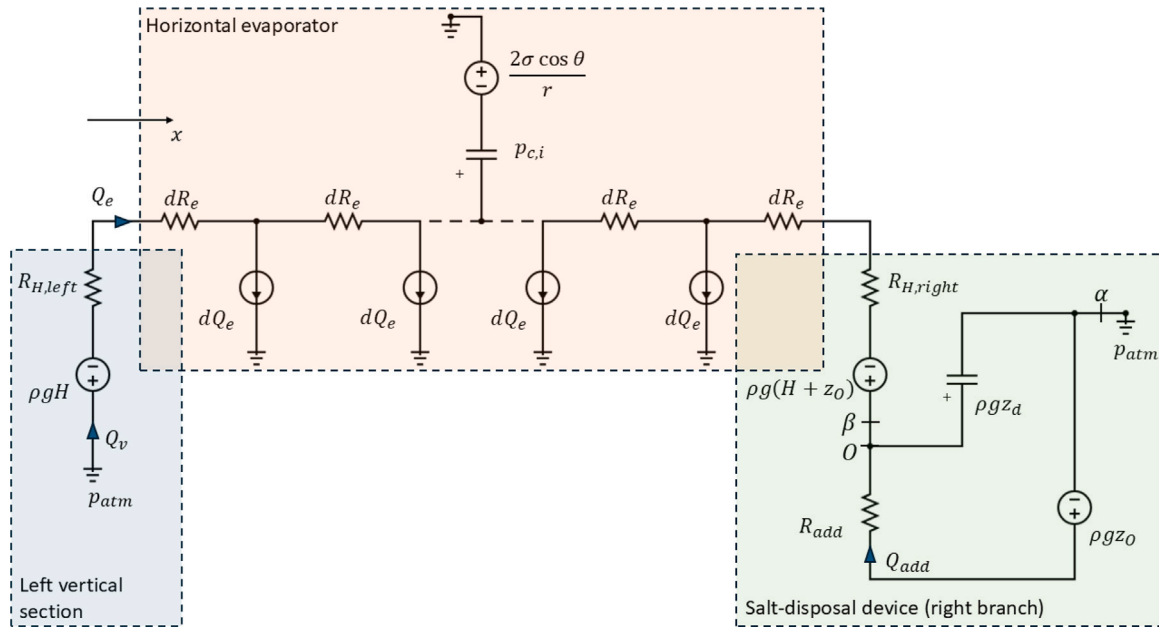


**Fig. 2.** Equivalent circuit representation of the proposed passive distillation device using the electric–hydraulic analogy. Shaded boxes identify the three subsystems discussed in the text: the horizontal evaporator (orange), the left vertical section (blue), and the salt-disposal device (green). All ground symbols denote the same reference pressure  $p_{atm}$ . Circuit parameters correspond to those defined in the physical system shown in Fig. 1, mapping hydraulic resistances ( $R_{H,left}$ ,  $dR_e$ ,  $R_{H,right}$ ,  $R_{add}$ ), pressures ( $\rho gH$ ,  $\rho g(H + z_O)$ ,  $\rho gz_d$ ,  $\rho gz_O$ ,  $2\sigma \cos \theta / r$ ,  $p_{c,i}$ ), and flow rates ( $Q_v$ ,  $Q_e$ ,  $dQ_e$ ,  $Q_{add}$ ). From the Young–Laplace relation, the capillary element is modeled as a fixed pressure source  $\Delta p_{cap} = 2\sigma \cos \theta / r$  (with  $r$  the effective pore radius and  $\sigma$  the liquid–air surface tension, and  $\theta$  the static contact angle at the liquid–solid interface) in series with a capacitor generating  $p_{c,i}$ . The latter is an effective, model-derived pressure-like quantity that accounts for interfacial energy stored in the deformed meniscus whenever the available capillary pressure is not fully required to sustain the hydraulic head. Under transient increases in demanded pressure, this stored energy is released; when the demand decreases, the meniscus flattens and energy is stored again. To evaluate the equivalent pressure acting on the salt-disposal device, two conceptual terminals are defined,  $\alpha$  and  $\beta$ :  $\alpha$  coincides with the reference node (free surface at atmospheric pressure  $p_{atm}$ ) and  $\beta$  is the node in the porous right leg immediately upstream of the static pressure tap  $O$  (located at depth  $z_O$ ), i.e., just above the added hydraulic resistance  $R_{add}$ . Short-circuiting the ground nodes and open-circuiting these terminals allows us to perform the Thevenin reduction, yielding the circuit shown in Fig. C.1 (Appendix C).

within the salt-disposal device. In particular, the free-surface elevation  $z_d(t)$  in the disposal device (see Fig. 1) evolves over time before reaching steady state and is therefore modeled as a capacitor in the circuit analogy. Full and detailed derivations of the hydraulic resistances and the governing equations are provided in Appendices A and B.

### 2.3. Thevenin equivalent model simplification

Fig. 2 presents the hydraulic schematic of the passive solar distillation system, derived using the electric–hydraulic analogy and assuming that dynamic pressure is negligible relative to other pressure contributions (see Appendix B, for details on the validity of this assumption). From this schematic, the Thevenin equivalent circuit can be derived and thus the Thevenin equivalent pressure difference  $\Delta p_{\alpha\beta,th}$  and resistance  $R_{\alpha\beta,th}$  between the two terminals  $\alpha$  and  $\beta$ , which bound the salt-disposal branch (see Appendix C). Based on these quantities, the steady-state hydraulic head in the capacitor ( $z_d$ ) is obtained, where steady-state quantities are denoted by the subscript “eq”:

$$\begin{aligned} \Delta z_{d,eq} = z_O - z_{d,eq} &= \frac{R_{add} \Delta p_{\alpha\beta,th} + \rho g z_O}{\rho g R_{\alpha\beta,th} + R_{add}} = \\ &= \frac{4\mu\tau^2}{eg\rho^2 r^2} \frac{\eta \frac{q_{sun}}{s} L}{h_{gl}(T) - c_{p,w}T} \frac{2H + L}{1 + \frac{r_{add}^2}{r^2} \frac{2H + L + z_O}{H_{add}}}, \end{aligned} \quad (5)$$

where  $\rho$  is the fluid density,  $g$  the gravitational acceleration; then the parameters  $q_{sun}$ ,  $s$  and  $L$  correspond solar irradiance, evaporator thickness and length, respectively. Importantly,  $\eta$  denotes an effective evaporation efficiency that lumpedly accounts not only for optical losses, but also for any energy losses associated with non-isothermal effects in the porous evaporator, including conductive heat diffusion to

the seawater thermostat and sensible heat advection required to warm the incoming liquid. As a result,  $\eta$  quantifies the fraction of absorbed solar power that is ultimately converted into latent heat of evaporation. Additionally,  $h_{gl}$  latent heat of vaporization,  $c_{p,w}$  specific heat capacity of water, and  $T$  refers to the temperature of the porous medium. Then,  $H$  is the height of the section,  $r_{add}$  and  $H_{add}$  represent the pore radius and length of the additional high hydraulic resistance (see Fig. 1a). Finally,  $z_O$  represents the depth at which the connection between the porous medium and the salt disposal device is established (see Fig. 1a). For clarity, a complete list of symbols and units is provided in Appendix E (Nomenclature). This model captures the coupling between the fluid velocity in the porous network (and the resulting viscous losses) and the evaporative flux driven primarily by solar irradiance  $q_{sun}$ . Crucially, this coupling leads to  $\Delta z_{eq}$ , which is the quantity modeled in Eq. (5). The full derivation is provided in Appendix C.

Assuming that the pore radius of the additional resistance is several orders of magnitude smaller than the pore radius of the remaining porous material, i.e.,  $r_{add} \ll r$ , the simplified expression of Eq. (5) becomes

$$\Delta z_{d,eq} \approx \frac{4\mu}{\rho^2 g (h_{gl}(T) - c_{p,w}T)} \left(\frac{\tau L}{r}\right)^2 \left(1 + 2\frac{H}{L}\right) \frac{\eta q_{sun}}{cs}. \quad (6)$$

To evaluate the temporal evolution of the water level in the capacitor (i.e., the salt-disposal pocket), in addition to the steady-state hydraulic head difference  $\Delta z_{d,eq}$ , it is essential to assess the characteristic time constant governing water accumulation and release. The temporal evolution of  $z_d(t)$  follows the first-order RC (see Fig. C.2b in Appendix C) differential equation:

$$\dot{z}_d + \frac{\rho g}{R_{\alpha\beta} S_d} z_d = \frac{\Delta p_{eff}}{R_{\alpha\beta} S_d}, \quad (7)$$

where  $\Delta p_{eff}$  represents an effective pressure source that varies between daytime and nighttime according to the operating conditions, specifically the presence or absence of evaporative flow. At rest, in the absence of evaporation,  $\Delta p_{eff} = \rho g z_O$  (as predicted by the Thevenin equivalent) and  $z_d = z_O$ . During daytime, evaporation lowers  $\Delta p_{eff}$  relative to its rest value and thereby decreasing  $z_d$  and establishing a positive hydraulic head difference  $\Delta z_d = z_O - z_d$  (piezometer-like behavior). At night, when evaporation ceases,  $\Delta p_{eff}$  rises back to  $\rho g z_O$  and  $z_d$  relaxes toward  $z_O$ , allowing backflow thus pocket refilling and the gradual decay of  $\Delta z_d$ . The transient evolution of  $z_d$ , described by the first-order differential equation Eq. (7), is characterized by the time constant:

$$\tau_{ch} = \frac{R_{\alpha\beta} \cdot S_d}{\rho g} = \frac{8\mu}{\rho g} \left( \frac{\tau L}{r} \right)^2 \left( 1 + 2 \frac{H}{L} + \frac{z_O}{L} \right) \frac{S_d}{\epsilon s B L}, \quad (8)$$

yielding

$$\Delta z_d(t) = \Delta z_{d,eq} \left( 1 - e^{-\frac{t}{\tau_{ch}}} \right). \quad (9)$$

Considering the magnitude of the involved parameters,  $\tau_{ch}$  can be on the order of hundreds of hours, which is significantly greater than the operational time  $t$  of the solar distiller, typically on the order of few hours. Under the assumption  $\frac{t}{\tau_{ch}} \rightarrow 0$ , Eq. (9) can be then linearized by Taylor expansion:

$$\begin{aligned} \Delta z_d(t) &\approx \Delta z_{d,eq} \frac{t}{\tau_{ch}} = \\ &= \frac{\eta q_{sun} \left( 1 + 2 \frac{H}{L} \right)}{2 \rho (h_{gl}(T) - c_{p,w}T) \left( 1 + 2 \frac{H}{L} + \frac{z_O}{L} \right) \frac{S_d}{BL}} t \end{aligned} \quad (10)$$

All symbols appearing in the formulation are summarized in Appendix E (Nomenclature). To evaluate the performance of the spontaneous salt-removal device, the rinse number is introduced and defined as a dimensionless metric that quantifies how many times the effective evaporator volume ( $V_{ol_e}$ ) is replenished by the siphon-driven flow from the salt-disposal device ( $V_{ol_d}$ ):

$$n_R = \frac{V_{ol_d}}{V_{ol_e}} = \frac{\Delta z_d S_d}{\epsilon s B L}. \quad (11)$$

Moreover, considering Eq. (10), the number of complete rinsing events per operational time can be expressed as:

$$\frac{n_R}{t} = \frac{\eta q_{sun}}{2 \epsilon s \rho (h_{gl}(T) - c_{p,w}T)} \frac{1 + 2 \frac{H}{L}}{1 + 2 \frac{H}{L} + \frac{z_O}{L}}. \quad (12)$$

Overall, the model predicts the steady-state hydraulic head difference, its simplified expression, the characteristic time constant, the transient evolution of  $z_d$ , and the rinse number. Further details and derivations are provided in Appendix C.

#### 2.4. Experimental validation

The configuration shown in Fig. 1 represents the conceptual design of the passive siphon-driven salt removal introduced in this work. For experimental validation of the proposed hydraulic model, however, a simplified proof-of-concept layout was implemented (see Figs. 3a,b) to facilitate fabrication.

This experimental configuration differs from the conceptual design in that the hydraulic resistance  $R_{H,right}$  no longer accounts for the entire segment  $z_O$ , but only for the portion  $\Delta z_d$ . This modification arises from the removal of the porous medium impermeable walls. As a consequence, the segment  $\Delta z_d$  remains hydraulically active, since it is not submerged, whereas the lower part of the leg is fully immersed and thus offers negligible flow resistance. Consequently, the expression for the hydraulic resistance on the right-hand side becomes

$$R_{H,right} = \frac{8\mu\tau^2}{\epsilon Ar^2} (H + \Delta z_d). \quad (13)$$

Moreover, since the pore radius of the additional resistance is  $r_{add} = 0$  and there is no direct connection to the sea, the associated hydraulic

resistance  $R_{add}$  can be considered infinite. Under these conditions, as in Eq. (6), the equilibrium hydraulic head difference becomes:

$$\Delta z_{d,eq} = \frac{4\mu}{\rho^2 g (h_{gl}(T) - c_{p,w}T)} \left( \frac{\tau L}{r} \right)^2 \left( 1 + 2 \frac{H}{L} \right) \frac{\eta q_{sun}}{\epsilon s}. \quad (14)$$

A disadvantage of such siphon experimental implementation, which lacks the additional hydraulic resistance and a direct seawater connection with respect to the layout in Fig. 1, is its inability to discharge accumulated salt from the disposal compartment. However, this issue could be mitigated by implementing one-way valves or designing engineered techniques for selective salt release, without compromising the device's performance.

In this proof-of-concept implementation, the expressions for the key variables are accordingly modified. In the original configuration, although  $R_{eff}$  depended on  $R_{H,right}$ , the latter was constant in time (Appendix A, Eq. (A.8)), and thus  $R_{eff}$  was also constant. In the present configuration, instead,  $R_{H,right}$  depends explicitly on  $\Delta z_d(t) = z_O - z_d(t)$ , so that  $R_{eff}$  varies with time and Eq. (7) becomes nonlinear:

$$\dot{z}_d + \frac{\rho g}{R_{eff}(z_d) S_d} z_d = \frac{\Delta p_{eff}}{R_{eff}(z_d) S_d}. \quad (15)$$

As shown in Eq. (C.18) (see Appendix C), for  $r_{add} = 0$  the effective resistance reduces to the Thevenin resistance, i.e.  $R_{eff} \approx R_{\alpha\beta,th}$ , which reads:

$$R_{\alpha\beta,th} = \frac{8\mu\tau^2}{\epsilon Ar^2} L \left( 1 + 2 \frac{H}{L} + \frac{\Delta z_d}{L} \right). \quad (16)$$

Assuming  $\Delta z_d \ll L$ , the ratio  $\Delta z_d/L$  can be neglected. In this limit,  $R_{eff}$  simplifies to a constant value:

$$R_{eff} \approx \frac{8\mu\tau^2}{\epsilon Ar^2} L \left( 1 + 2 \frac{H}{L} \right). \quad (17)$$

Consequently,  $R_{eff}$  can be regarded as constant, and the governing differential equation reduces to a linear form, as in the original configuration. In this case, the characteristic time  $\tau_{ch}$  is derived from the linearized form of Eq. (15):

$$\tau_{ch} = \frac{R_{eff} S_d}{\rho g} = \frac{8\mu}{\rho g} \left( \frac{\tau L}{r} \right)^2 \left( 1 + 2 \frac{H}{L} \right) \frac{S_d}{\epsilon s B L}. \quad (18)$$

In the initial stages, when  $\frac{t}{\tau_{ch}} \rightarrow 0$ , Eq. (9) can be linearized again via a first-order Taylor expansion. Furthermore, if  $\tau_{ch}$  is sufficiently large – i.e., several orders of magnitude greater than a typical operational timescale of 8 h – the linearized model can accurately capture the whole daily behavior of the device. In this limit, the temporal evolution of the hydraulic head difference in the salt-disposal device becomes:

$$\Delta z_d(t) \approx \Delta z_{d,eq} \frac{t}{\tau_{ch}} = \frac{\eta q_{sun}}{2 \rho (h_{gl}(T) - c_{p,w}T) \frac{S_d}{BL}} t. \quad (19)$$

Besides, the number of complete rinsing events per unit time can be expressed according to Eq. (11) as:

$$\frac{n_R}{t} = \frac{1}{2 \rho (h_{gl}(T) - c_{p,w}T)} \frac{\eta q_{sun}}{\epsilon s}. \quad (20)$$

The experimental test rig used for validation is illustrated in Figs. 3c and d. Its primary purpose is to measure the evaporation-induced hydraulic head difference  $\Delta z_d(t)$  and compare it with the model predictions (Eq. (19)). The head difference is not measured directly but inferred from the time-resolved mass loss of a beaker (component 3 in Fig. 3c), which is converted into the corresponding hydraulic head.

Solar irradiance is mimicked by a heat source placed beneath the porous evaporator (hydrophilic cloth). In detail, heating is provided by two electrical resistance mats (RS PRO Silicone Heater Mat) with a total area of 25 cm<sup>2</sup>, connected in parallel and powered by a DC supply (Teledyne LeCroy T3PS). The effective heat absorption efficiency was determined experimentally as  $\eta = 0.52 \pm 0.03$  by running control tests without the seawater reservoir and measuring the mass of water evaporated from the beaker. Mass variation during each experiment was continuously recorded with a precision balance (Kern PCB).

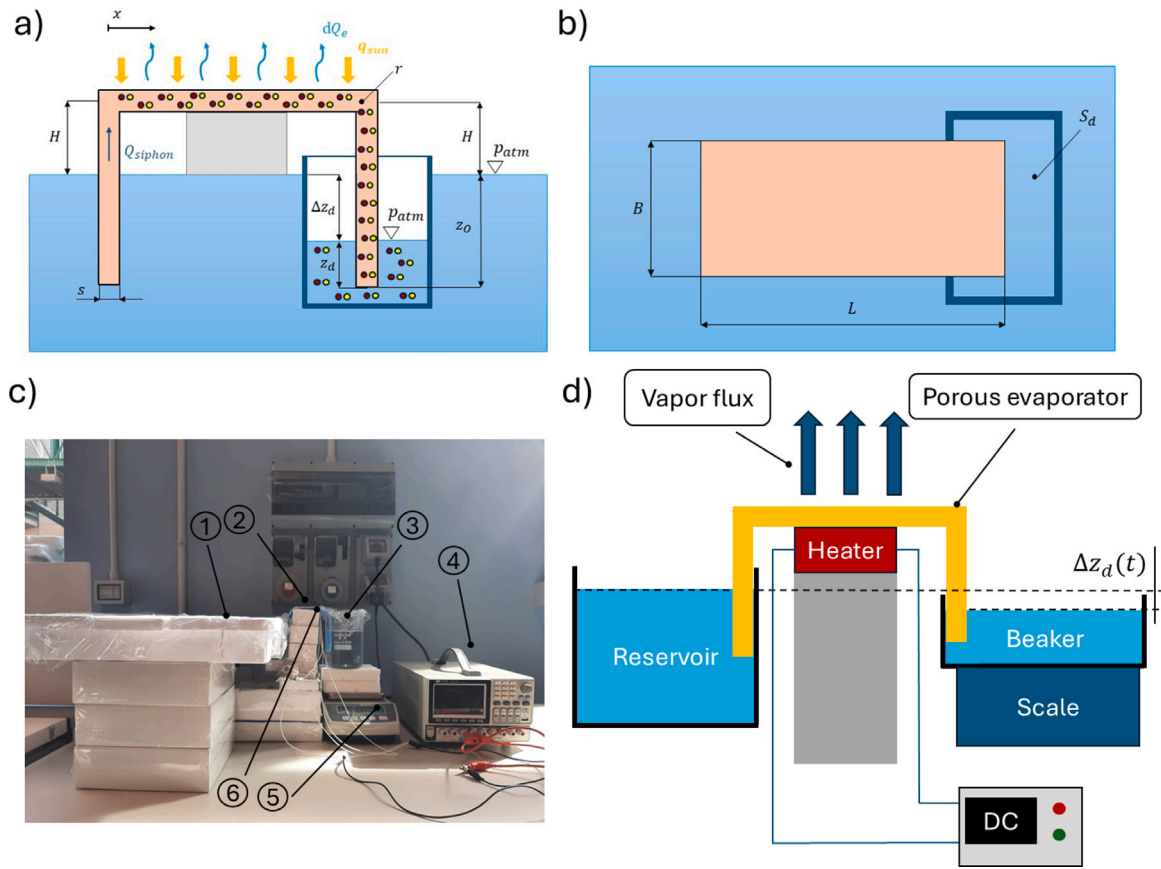


**Fig. 3.** Experimental proof-of-concept of the spontaneous salt-disposal device integrated with the evaporation-based passive distillation system. (a) Sectional view of the inverted U-shaped porous evaporator coupled to the spontaneous salt-disposal pocket. Unlike the conceptual design, in the experimental proof-of-concept, the right vertical leg lacks impermeable walls and additional hydraulic resistance, thus preventing direct connection with the sea. The key geometric parameters are highlighted: the horizontal evaporator is positioned at height  $H$  above sea level, with porous medium thickness  $s$  and pore radius  $r$ . The right end of the porous medium is located at a depth  $z_O$ , while the water level inside the salt-disposal device reaches  $z_d$ , introducing the hydraulic head difference  $\Delta z_d = z_O - z_d$ . The reference coordinate system  $x$  is shown. Solar irradiance  $q_{sun}$  induces localized evaporation  $dQ_e$ , resulting in salt accumulation within the impermeable-walled salt-disposal device, with no direct discharge path. (b) Top view showing evaporator dimensions (width  $B$ , length  $L$ ) and the disposal section  $S_d$ . (c) Photograph of the experimental setup used for validation, which consists of the following elements: (1) saline water reservoir, (2) porous evaporator (hydrophilic cloth), (3) beaker, (4) DC power supply, (5) precision scale, (6) electric heater. (d) Schematic illustration of the experimental test rig.

To reproduce the seawater boundary condition, the beaker (component 3 in Fig. 3c) was hydraulically connected to a large reservoir of artificial seawater (component 1 in Fig. 3c) through the porous evaporator. The hydrophilic cloth is characterized by  $\epsilon = 0.75 \pm 0.05$ ,  $r = 100 \pm 25 \mu\text{m}$ , and  $s = 0.1 \pm 0.05 \text{ cm}$ . Each experiment began with a 24 h preconditioning phase, during which the setup was covered to suppress environmental evaporation and allow equilibration. At the end of this stage, no measurable mass variation was observed in the beaker, confirming  $\Delta z = 0 \text{ mm}$  between the beaker and the reservoir. The cover was then removed, heating initiated, and the experiment run for approximately 2 h while continuously recording beaker mass. Finally, the mass-loss curve was converted into  $\Delta z_d(t)$  by dividing the measured mass variation by the water density  $\rho$  and the section of the beaker.

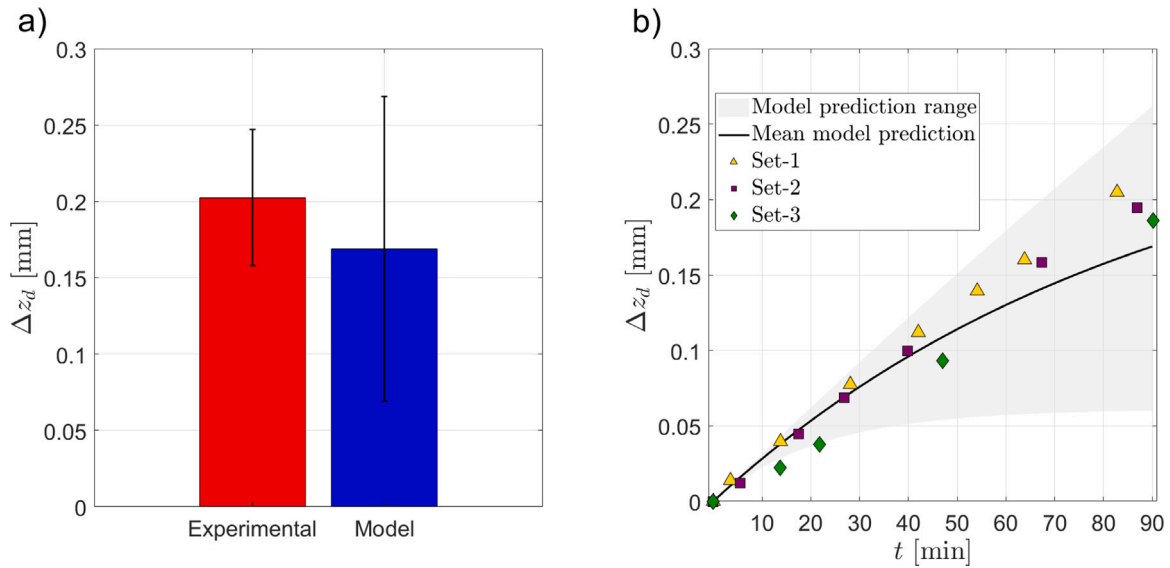
### 3. Results

This section presents the main results of the study. First, the analytical model is validated against experimental measurements obtained with the laboratory prototype. Subsequently, the applicability of the proposed mechanism is evaluated through a case study involving a passive solar distillation device. The analysis is then extended to scalability constraints and generalized design guidelines derived from the linearized model.

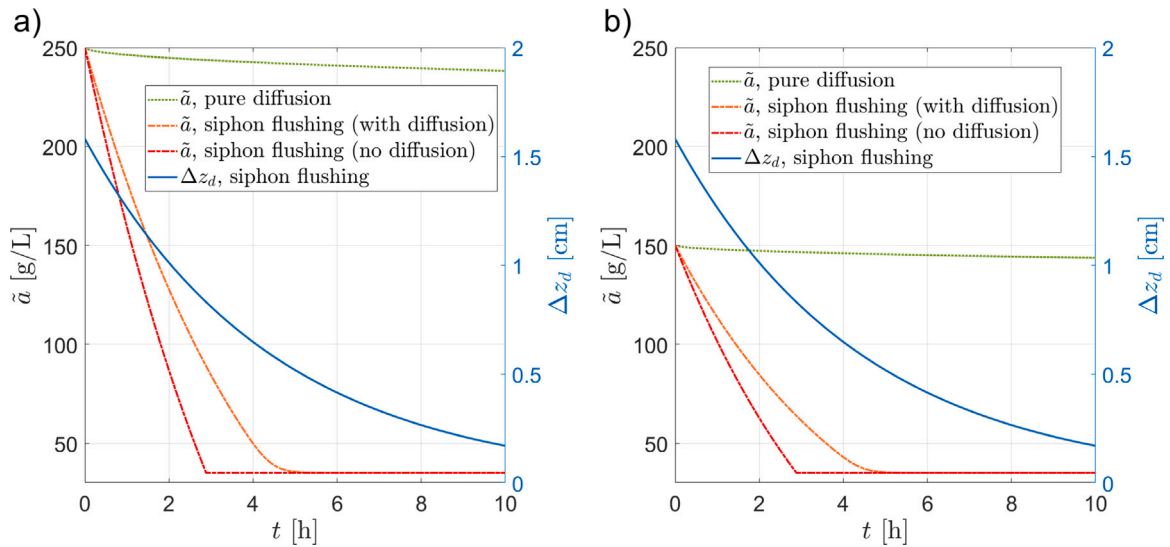
#### 3.1. Validation of the model

Fig. 4 summarizes the validation of the analytical model. Fig. 4a compares predicted and measured values of  $\Delta z_d$  after 90 min of operation. Experimental data are reported as mean value with 95% confidence interval, derived from three independent tests using Student's  $t$ -distribution. Model uncertainty was obtained by propagating input-parameter uncertainties through the general (non-linearized) form of Eq. (9). To obtain the experimental value at 90 min, a linear interpolation was performed between the two experimental measurements immediately preceding and following this time. This procedure was repeated for the three independent test sets, resulting in three interpolated values at the 90-minute mark. At  $t = 90 \text{ min}$ , the analytical model predicts  $\Delta z_d = 0.17 \text{ mm}$  (range: 0.06–0.26 mm), corresponding to an uncertainty of  $\pm 0.10 \text{ mm}$ . The experimental value is  $0.202 \pm 0.044 \text{ mm}$  (mean  $\pm 95\% \text{ CI}$ ,  $n = 3$ ). The relative deviation between the two mean values is approximately 15%, indicating good agreement. The model slightly underestimates  $\Delta z_d$  within the observed timeframe, a discrepancy primarily associated with the characteristic time  $\tau_{ch}$ , whose sensitivity to uncertain parameters becomes significant at the chosen reference time.

Panel (b) compares the full time evolution of  $\Delta z_d$ . The solid black line corresponds to predictions using nominal parameter values (i.e.,



**Fig. 4.** Model validation against experimental data under operating conditions:  $q_{um} = 1000 \text{ W m}^{-2}$ ,  $H = 3 \pm 1 \text{ cm}$ ,  $s = 0.1 \pm 0.05 \text{ cm}$ ,  $\epsilon = 0.75 \pm 0.05$ ,  $r = 100 \pm 25 \text{ }\mu\text{m}$ , and  $\eta = 0.52 \pm 0.03$ . (a)  $\Delta z_d$  after 90 minutes: the blue bar represents the mean analytical prediction, with uncertainty estimated as half the min–max interval resulting from input-parameter variations. The red bar indicates the mean experimental value at 90 min, with error bars corresponding to the 95% confidence interval (Student's  $t$ -distribution,  $n = 3$ ). (b) Temporal evolution of  $\Delta z_d$ : analytical prediction (black line) with uncertainty gray band versus experimental measurements. Distinct symbols and colors correspond to independent experimental test repetitions. The  $x$ -axis represents time (min), and the  $y$ -axis shows  $\Delta z_d$  (mm).



**Fig. 5.** Performance of siphon-induced flushing for salt removal. (a) Time evolution of the average salt concentration in the evaporator  $\bar{a}$  (left  $y$ -axis) and hydraulic head difference  $\Delta z_d$  (right  $y$ -axis) for an initial concentration of  $\bar{a}(0) = 250 \text{ g/L}$ , comparing pure diffusion and siphon-induced flushing. For siphon flushing, both an ideal advection-only model (neglecting diffusion during flushing) and an advection-diffusion model (including diffusion during flushing) are reported. (b) Same analysis for an initial concentration of  $\bar{a}(0) = 150 \text{ g/L}$ . Including diffusion smooths the concentration front and removes the non-differentiable corner observed in the advection-only approximation, while only mildly affecting the overall rinsing performance.

the central values within their uncertainty ranges), while the shaded region represents the uncertainty envelope. The lower bound corresponds to parameter sets that minimize  $\Delta z_d$ —reducing  $\tau_{ch}$  and accelerating the transient, whereas the upper bound increases  $\tau_{ch}$ , producing a slower approach to steady state. The experimental trend shows progressive flattening, indicating the onset of steady-state conditions and confirming that the characteristic time is comparable to the experimental duration.

Overall, the agreement between analytical predictions and experimental observations confirms the model's validity and its ability to capture the dominant physical mechanisms governing  $\Delta z_d(t)$ .

### 3.2. Case study: Application to a passive solar distillation device

The salt removal capability of the proposed passive siphon-based system was assessed considering as case study the passive solar distiller developed by [Chiavazzo et al. \(2018\)](#). The validated hydraulic model was parameterized with standard water properties: dynamic viscosity  $\mu = 8.9 \times 10^{-4} \text{ Pa s}$ , density  $\rho = 1000 \text{ kg m}^{-3}$ , latent heat of vaporization  $h_{gl} = 2.26 \times 10^6 \text{ J kg}^{-1}$ . The porous evaporator dimensions were  $12 \times 12 \text{ cm}^2$  with 1 mm thickness ([Chiavazzo et al., 2018](#)), elevated  $H = 4 \text{ cm}$  above the seawater level. The material of the porous evaporator was assumed to be a woven cotton fabric with a hydraulic pore diameter

$D_h \approx 50 \mu\text{m}$  and porosity  $\epsilon \approx 75\%$  (Zupin et al., 2024) (fabric code R 2/4 29.3/20). The characteristic pore radius was taken as  $r = D_h/2 \approx 25 \mu\text{m}$ . The cross-sectional area of the salt-disposal device was assumed to be a fraction of the evaporator area, namely  $S_d = 0.1BL$ , where  $B$  and  $L$  are the width and length of the evaporator, respectively. An effective absorbed solar irradiance  $\eta q_{sun}$  of  $600 \text{ W m}^{-2}$  was assumed.

Based on these parameters, the system characteristic time constant was  $\tau_{ch} = 4.48 \text{ h}$  and the steady-state head difference  $\Delta z_{d,eq} = 2.14 \text{ cm}$ . According to the analytical model (see Eq. (9)), after 6 h of solar irradiation, the hydraulic head difference reaches  $\Delta z_d = 1.58 \text{ cm}$ , corresponding to a rinse number  $n_R = 2.11$ , as defined in Eq. (11). This indicates that the salt accumulated on the evaporator during the considered irradiation period could be completely rinsed at least once ( $n_R > 1$ ) as soon as evaporation process stops (e.g., during nighttime), confirming the effectiveness of the passive siphon-based system for autonomous, energy-free salt management.

To further compare the efficiency of the siphon-induced flushing mechanism against pure diffusion, the average salt concentration in the evaporator,  $\bar{a}(t)$ , was evaluated under three transport assumptions: (i) diffusion only, (ii) siphon-driven flushing with advection-only transport (diffusion neglected during flushing), and (iii) siphon-driven flushing with coupled advection-diffusion transport during the discharge phase. The average concentration  $\bar{a}(t)$  was computed as the ratio between the total mass of salt contained within the porous evaporator and the actual volume of liquid present in the porous medium, i.e.  $\epsilon B L s$ , where  $\epsilon$  is the porosity and  $B$ ,  $L$ , and  $s$  are the width, length, and thickness of the evaporator, respectively.

The resulting  $\bar{a}(t)$  values, together with the time evolution of the hydraulic head difference  $\Delta z_d$ , are presented in Fig. 5, where panels a and b correspond to initial concentrations of  $\bar{a}(0) = 250 \text{ g L}^{-1}$  (near saturation condition) and  $\bar{a}(0) = 150 \text{ g L}^{-1}$ , respectively. In the diffusion-only scenario, salt decreases slowly, reaching  $238.1 \text{ g L}^{-1}$  and  $143.6 \text{ g L}^{-1}$  after 10 h for the two initial concentration values, respectively. In sharp contrast, siphon-induced flushing rapidly reduces the concentration to the seawater value within a few hours, regardless of the initial concentration value. In the idealized advection-only case (diffusion neglected during flushing), the seawater level is restored within 2.88 h. When diffusion is included during flushing (advection-diffusion model), the rinsing remains highly effective, although the complete concentration decay becomes 1.2 h slower due to diffusive mixing at the flushing front. At  $t = 2.88 \text{ h}$ , the hydraulic head difference has decreased from its initial value of 1.58 cm (hydraulic head difference reached after 6 h of solar irradiation) to 0.83 cm. After 10 h of operation, the hydraulic head difference further decreases to 0.17 cm. This reduction in hydraulic head difference reflects the occurrence of multiple rinsing events: as predicted by  $n_R > 1$ , the system is able to perform more than one complete flushing over the considered time interval, ensuring excellent salt removal and evaporator cleanliness.

The initial sharp decrease in salt concentration observed during siphon-induced flushing is due to the high hydraulic head difference  $\Delta z_d$ , which enables a fast brine outflow. As the salt-disposal pocket fills and its free surface rises approaching sea level,  $\Delta z_d$  decreases, reducing the driving head and thus the flushing rate, thus resulting in a progressively gentler slope of the concentration curve. This dynamic accurately reflects the physical process whereby the rinsing efficiency is self-regulated by the available hydraulic gradient.

It is worth noting that the non-differentiable corner observed in the concentration curve (siphon-induced flushing case) corresponds to the moment when the flushing front reaches the outlet of the evaporator (at  $x = L$  in Fig. 1a), meaning that the entire internal volume has been fully rinsed. At this point, the expelled salt-enriched water is rapidly replaced by ambient seawater, which acts as the flushing fluid. This abrupt replacement produces the sharp corner in the concentration curve. When diffusion is included during siphon-driven flushing (advection-diffusion model in Fig. 5), the salinity front is progressively spread, the corner disappears, and the concentration evolution becomes smooth. In this

more realistic case, diffusion mildly reduces the rinsing performance, since salt is partially transported back toward the evaporator from nearby higher-concentration regions during the replacement process. Importantly, this adverse diffusive mixing can be straightforwardly counteracted at the design level by targeting a rinse number slightly above unity ( $n_R > 1$ ). This guarantees complete regeneration even in the presence of diffusion, while preserving the fully passive nature of the mechanism.

These results highlight not only the superior performance of siphon-induced hydraulic flushing for salt removal, but also its independence from the initial concentration in the evaporator, making it robust even for highly concentrated brines. For comparison, Xia et al. (2019) demonstrated continuous steam generation with edge-preferential crystallization and gravity-assisted salt harvesting for 600 h, with evaporation rates of  $1.05\text{--}1.42 \text{ kg m}^{-2} \text{ h}^{-1}$  at 3.5 wt% NaCl under 1 sun. A Janus 3D graphene evaporator maintained stable operation without salt accumulation up to 10 wt% brine, delivering  $1.71 \text{ kg m}^{-2} \text{ h}^{-1}$  under 1 sun (Yang et al., 2023). Stincone et al. (2024) reported Marangoni-assisted salt rejection up to two orders of magnitude above diffusion, enabling overnight removal of accumulated salt with distillate rates of  $2 \text{ L m}^{-2} \text{ h}^{-1}$  under  $< 1$  sun. Zeng et al. (2019) demonstrated continuous osmotic pumping using a polyelectrolyte hydrogel foam, achieving stable evaporation rates of  $1.3 \text{ kg m}^{-2} \text{ h}^{-1}$  in 3.5 wt% NaCl under 1 sun for 72 h. Compared to these strategies, the key novelty of the present work is that salt removal occurs through bulk advective regeneration of the porous evaporator via siphon flushing, autonomously triggered by evaporation-induced hydraulic head. This provides a robust, scalable, and interfacial-independent salt-management approach, capable of restoring seawater-level salinity within a few hours.

### 3.3. Scalability and size constraints

An important question for practical deployment concerns the maximum evaporator length  $L$  that can be operated without salt clogging or performance degradation. This limit is governed by two distinct and conceptually independent constraints: (i) a capillary dry-out limit,  $L_{dry-out}$ , which ensures continuous wetting of the porous evaporator, and (ii) a siphon-regeneration limit,  $L_{lim,siphon}$ , which requires that the siphon-driven discharge is sufficiently fast to flush the porous volume during a rinsing event.

The dry-out constraint  $L_{dry-out}$  is intrinsic to capillary-fed evaporators and has been extensively analyzed in our previous works (Meo and Morciano, 2022; Meo et al., 2023). Those studies provide quantitative design guidelines for wick thickness (typically in the millimeter range) and geometry to prevent dry-out and premature salt crystallization, and predict feasible evaporator lengths up to the order of meters under realistic solar operating conditions.

The present analysis therefore focuses on the siphon-regeneration constraint  $L_{lim,siphon}$ . Importantly, the dominant limitation associated with siphon operation is generally not the ability to generate the hydraulic head required to trigger siphon activation. For a fixed operational time  $t_{op}$ , a target head difference  $\Delta z_{target}$  can always be achieved by appropriately tuning the geometrical ratio  $S_d/(BL)$ , within reasonable design bounds. Instead, the critical constraint is associated with the discharge phase, namely the requirement that at least one full evaporator volume is flushed within the available discharge time  $t_{dis}$ .

By combining the governing relations of the model and considering the asymptotic regime  $\tau_{ch} \gg t_{op}$  (i.e., large systems), the maximum sustainable evaporator length for effective siphon-driven regeneration,  $L_{lim,siphon}$ , can be expressed as:

$$\begin{aligned} & \left( \frac{\tau L_{lim,siphon}}{r} \right)^2 \frac{1 + 2H/L}{\epsilon s} = \\ & = \frac{t_{dis}}{\frac{8\mu S_d}{\rho g BL} \ln \left( 1 - \frac{2\rho(h_{gl}(T) - c_{p,w}T)}{\eta q_{sun}} \frac{\epsilon s}{t_{op}} \right)} \end{aligned} \quad (21)$$

All symbols are defined in Appendix E. Eq. (21) highlights that the siphon-related size limit is primarily controlled by viscous losses (hydraulic resistances) in the porous medium and by the volume of liquid to be flushed, rather than by the capability of generating the triggering hydraulic head.

The trends predicted by Eq. (21) are physically intuitive. Smaller pore radii  $r$  reduce  $L_{lim,siphon}$  by increasing the hydraulic resistance and slowing down the discharge flow. Similarly, increasing the porous thickness  $s$  decreases  $L_{lim,siphon}$ , since a thicker wick stores a larger liquid volume that must be flushed (at least one complete rinse) within the available discharge time  $t_{dis}$ .

Using representative design parameters (e.g.,  $S_d/(BL) \approx 0.1$ ,  $s$  in the millimeter range, and  $r$  between tens and hundreds of micrometers), Eq. (21) predicts  $L_{lim,siphon}$  values typically on the order of meters (e.g., 0.5–2 m depending on  $r$  and  $s$ , and larger for larger pore sizes). Consequently, depending on operating conditions and design choices, the siphon-related constraint can be comparable to or less restrictive than the dry-out limit  $L_{dry-out}$ , indicating that siphon regeneration is generally not the dominant scalability bottleneck.

To provide a concrete and quantitative demonstration of scalability, we consider a device similar to that analyzed in Section 3.2 but on meter-scale, with  $L = 1$  m,  $B = 0.5$  m,  $r = 25$   $\mu\text{m}$ ,  $\epsilon = 0.75$ ,  $s = 2$  mm,  $H = 4$  cm,  $\eta = 0.6$ , and  $q_{sun} = 1000$   $\text{W m}^{-2}$ , operated under a 10 h irradiation phase followed by 14 h discharge. Using the capillary-driven transport model of Ref. Meo and Morciano (2022), the dry-out limit is found to be  $L_{dry-out} \approx 2.1$  m, confirming that a 1 m evaporator remains safely below the capillary constraint. Imposing a conservative regeneration criterion  $n_R > 1.5$  yields a geometrical ratio  $S_d/(BL) = 0.008$ , corresponding to a characteristic time  $\tau_{ch} = 8.2$  h. Under the assumed daily cycle, the hydraulic head available for siphon flushing, computed from the full transient evolution during both evaporation and discharge, reaches approximately  $\Delta z_d \approx 28$  cm and ensures  $n_R = 1.506$  over the cycle. The resulting disposal-pocket area remains geometrically reasonable,  $S_d = 0.004$   $\text{m}^2$ , with  $S_d/(Bs) = 4$ , thus avoiding extreme aspect ratios or impractical design constraints. This example demonstrates that a 1 m evaporator operates safely below the dry-out limit, autonomously generates a substantial evaporation-induced hydraulic head under realistic transient solar cycles, and satisfies a conservative rinsing requirement without restrictive geometrical conditions. Therefore, the proposed fully passive siphon-driven regeneration strategy does not exhibit intrinsic scalability limitations at the meter scale.

An additional aspect relevant for large-scale operation concerns the progressive increase of salinity within the salt-disposal pocket during prolonged evaporation. As freshwater is produced and brine is displaced into the pocket, salt accumulates in the disposal compartment. Importantly, the geometrical constraint associated with siphon activation, namely the ratio  $S_d/(BL)$ , applies only to the activation region near the free surface where the hydraulic head is generated. Below this region, the pocket cross-section can be enlarged without affecting siphon triggering. This decoupling provides design freedom to increase total storage volume independently of the activation geometry, thereby mitigating salinity rise through volumetric dilution. To quantify this effect for the representative 1 m device, the evaporative mass flux per unit length follows Eq. (C.2). Integration over the full evaporator length, assuming 10 h daily irradiation, yields a daily freshwater production of approximately 4.8 L. For seawater salinity  $c_{sea} = 35$   $\text{g L}^{-1}$ , this corresponds to a daily salt accumulation of about 0.17 kg, or roughly 1.2 kg after one week of autonomous operation. If the disposal pocket is designed with a total volume  $V_{pocket} = 10$  L, achievable by enlarging the lower storage region beneath the activation section, the resulting concentration after one week becomes  $c_{pocket} \approx 150$   $\text{g L}^{-1}$ . This value remains well below the NaCl solubility limit at ambient temperature, approximately 350  $\text{g L}^{-1}$ , thus preventing crystallization within the pocket. At such concentrations the increase in brine viscosity and density remains moderate, introducing only second-order

corrections to hydraulic resistance and not altering the qualitative mechanism of evaporation-driven head generation, which primarily depends on geometric ratios. Consequently, simple volumetric design enables multiple autonomous regeneration cycles over extended periods before any manual intervention is required. Beyond this first-level mitigation strategy, long-term brine management can be supported by passive concepts such as density-driven release, diffusive transport through hydraulically resistive salt-permeable interfaces, or one-way hydraulic elements. These system-level strategies are decoupled from the evaporator-regeneration mechanism demonstrated here and can be integrated without modifying the autonomous siphon activation process.

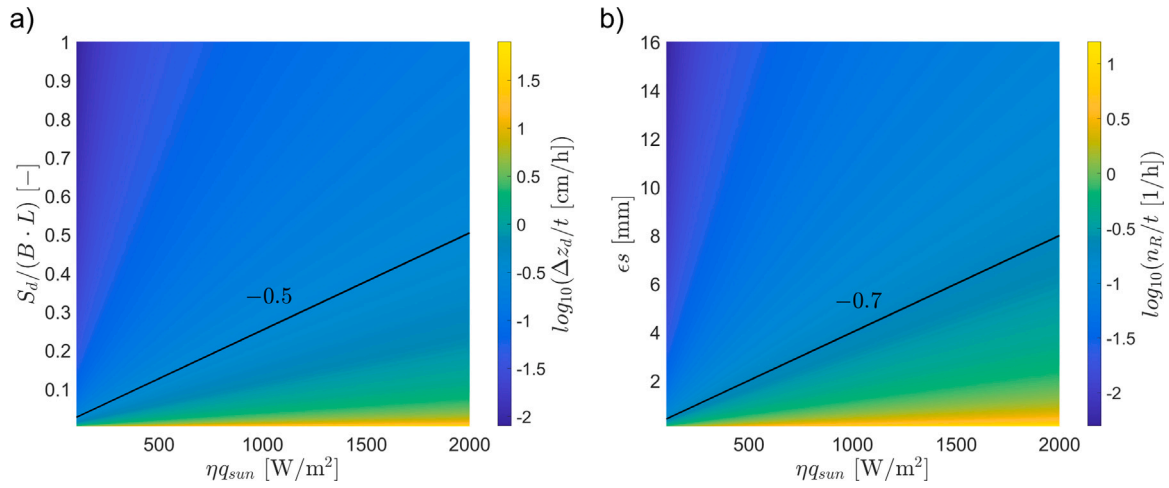
### 3.4. Generalization through the linearized model

The following results are based on the linearized model of the experimental configuration, as detailed in Eqs. (10) and (12). As discussed, linearization is valid when the characteristic time constant  $\tau_{ch}$  exceeds the operational timescale (a few hours) by at least two orders of magnitude, ensuring that the hydraulic head temporal evolution  $\Delta z_d(t)$  in the salt-disposal device is accurately captured by the analytical framework. Device performance is quantified using two key metrics: the hydraulic head difference  $\Delta z_d$  and the number of siphon-induced rinsing events  $n_R$ , both normalized per hour of solar irradiation. These metrics are critical for promoting regular brine removal and preventing salt accumulation in the evaporator.

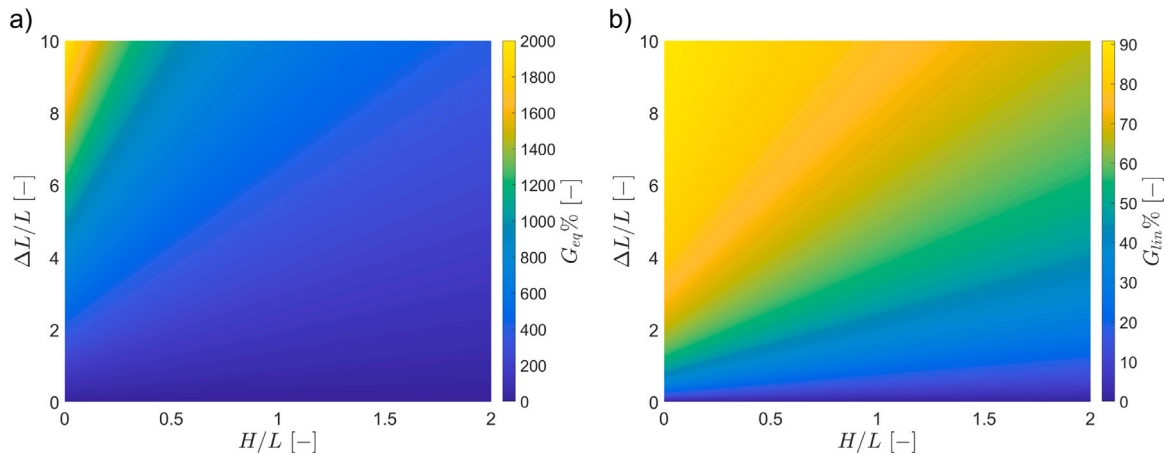
Fig. 6a illustrates how the accumulated hydraulic head difference per hour,  $\Delta z_d/t$ , depends on the effective solar irradiance  $\eta q_{sun}$  and the device area ratio  $S_d/(BL)$  (where  $S_d$  is the assumed uniform cross-sectional area of the salt-disposal device and  $BL$  is the evaporator footprint). As expected, higher solar irradiance increases  $\Delta z_d$ , thereby enhancing the hydrostatic pressure available to drive the siphon-induced flow for brine removal. A higher  $\Delta z_d$  also enables a larger brine storage volume within the salt-disposal device before discharge. For effective siphon operation, the accumulated head should reach a few centimeters over 8 h, corresponding to a logarithmic threshold of  $\log_{10}(2.5 \text{ cm}/8 \text{ h}) \approx -0.5$ . This reference value of 2.5 cm should be regarded as an order-of-magnitude estimate. It originates from preliminary simulations indicating that, depending on the overall hydraulic resistance of the circuit, a head difference of roughly 1–2 cm is typically required to sustain a flushing flow sufficient to rinse the evaporator. Compact devices with large pores (low hydraulic resistance) may require even smaller  $\Delta z_d$ . Conversely, the linearized regime is obtained for large  $\tau_{ch}$ , which is generally associated with high  $R_{eff}$  in Eq. (18), and thus with higher overall hydraulic resistance. A more accurate estimate of the required head difference  $\Delta z_d$  for efficient rinsing will, however, require further investigation of the flushing phase. In particular, as previously discussed, the required  $\Delta z_d$  must be assessed in relation to the hydraulic resistance of the system to ensure that  $\Delta z_d$  can drive a sufficient flushing volume within the non-operating period. Finally, lower values of  $S_d/(BL)$  are preferred, as they promote head buildup and rinsing even under moderate solar irradiance.

Fig. 6b shows how the effective solar irradiance  $\eta q_{sun}$  and the effective porous-medium thickness  $\epsilon s$  affect the rinsing frequency  $n_R/t$ . The logarithmic scale of  $n_R/t$  highlights the operating conditions under which the siphon mechanism is sufficiently activated to guarantee regular flushing. For robust performance, at least one rinsing event per hour is desirable; adopting a practical threshold of 1.5 rinsing events over an 8-hour period yields a logarithmic benchmark of  $\log_{10}(1.5/8 \text{ h}) \approx -0.7$ . As expected, both higher  $\eta q_{sun}$  and smaller  $\epsilon s$  lead to higher rinsing frequencies, thereby supporting effective evaporator cleaning.

Overall, these results highlight two complementary design levers for sustained, passive brine removal: (i) promoting head buildup via a low area ratio  $S_d/(BL)$  (panel a) and (ii) increasing the rinsing frequency by reducing the effective porous-medium thickness  $\epsilon s$  while maintaining sufficient irradiance (panel b). Lower values of  $S_d/(BL)$



**Fig. 6.** (a) Contour map showing the accumulated hydraulic head difference per hour on a logarithmic scale,  $\log_{10}(\Delta z_d/t)$ , as a function of effective solar irradiance  $\eta q_{sun}$  (x-axis) and device area ratio  $S_d/(BL)$  (y-axis). Larger  $\Delta z_d$  values correspond to higher hydrostatic pressure and greater internal brine storage, both enhancing siphon-driven evaporator flushing. Optimal performance is achieved at high irradiance and low area ratio. The thick black line marks the practical activation threshold corresponding to  $\Delta z_d \approx 2.5$  cm accumulated over  $t = 8$  h, i.e.,  $\log_{10}(2.5 \text{ cm}/8 \text{ h}) \approx -0.5$ . (b) Contour map of rinsing frequency on a logarithmic scale,  $\log_{10}(n_R/t)$ , as a function of effective solar irradiance  $\eta q_{sun}$  (x-axis) and effective porous-medium thickness  $\epsilon_s$  (y-axis, in mm). Higher rinsing frequency, indicating more effective salt removal, is achieved with increased irradiance and smaller thickness. The thick black line marks the practical operating threshold of  $n_R \approx 1.5$  rinses over  $t = 8$  h, i.e.,  $\log_{10}(1.5/8 \text{ h}) \approx -0.7$ . The threshold  $n_R \approx 1.5$  is conservatively set above unity to account for residual salt and diffusion during flushing, which may partially drive salt back into the evaporator (see Fig. 5).



**Fig. 7.** Relative gains in hydraulic head difference as functions of the dimensionless parameters  $\Delta L/L$  and  $H/L$ . Here, steady state refers to the long-time limit, while linear regime denotes the early-time dynamics ( $t \ll \tau_{ch}$ ), where  $\Delta z_d(t) \approx (\Delta z_{d,eq}/\tau_{ch}) t$ . (a) Steady-state relative gain  $G_{eq}$  (in %). (b) Linear-regime relative gain  $G_{lin}$  (in %). In both cases, the gain increases monotonically with  $\Delta L/L$ , and decreases monotonically with  $H/L$ . Both  $G_{eq}$  and  $G_{lin}$  are induced by the added localized resistance  $R_{loc}$  (equivalently, by the extra porous length  $\Delta L$ ) and are reported with respect to the baseline device ( $\Delta L = 0$ ). At steady state,  $G_{eq}$  grows approximately as  $2\Delta L/L$ , reaching up to 2000% within the explored range. In the linear regime,  $G_{lin}$  asymptotically approaches 90% for large  $\Delta L/L$ , representing the theoretical upper limit.

promote reliable siphon activation by increasing the available head, while reducing the effective porous-medium thickness  $\epsilon_s$  lowers the required flushing volume ( $V_e = \epsilon_s BL$ ), thus increasing  $n_R/t$ . However, low  $\epsilon$  is undesirable, as it would suppress capillary transport and limit liquid supply to the evaporating interface. Hence,  $\epsilon$  should be optimized in conjunction with  $s$ , seeking a balance between efficient capillary flow and sufficient resistance for head buildup. Adequate solar irradiance remains essential to sustain both hydrostatic pressure and rinsing frequency. Collectively, these design guidelines provide a framework for long-term, maintenance-free operation of passive solar distillation systems.

### 3.5. Topological design modification to boost hydraulic difference

A simple and effective strategy to enhance the hydraulic head difference  $\Delta z_d$  is to modify the system topology by increasing the hydraulic

resistance of the left-hand branch,  $R_{H,left}$ . This branch supplies more water directly from the sea than the right-hand branch, where an additional resistance  $R_{add}$  is located. The two resistances,  $R_{add}$  and  $R_{H,left}$ , act synergistically while influencing opposite sides of the network. A sufficiently large  $R_{add}$  reduces the refill of the pocket from the sea, while an increased  $R_{H,left}$  forces the evaporator to draw a greater fraction of water from the pocket instead of the sea. In essence,  $R_{add}$  restricts inflow (i.e., pocket refilling), while  $R_{H,left}$  promotes outflow (i.e., pocket emptying); and together they contribute to a larger  $\Delta z_d$ .

A practical way to achieve this is to introduce a localized hydraulic resistance  $R_{loc}$  in series between the left vertical branch and the irradiated horizontal evaporator. The corresponding equivalent circuit is reported in Appendix D. For consistency with the porous-medium formulation,  $R_{loc}$  can be represented by an equivalent porous length

$\Delta L$  defined as

$$\Delta L = R_{loc} \frac{\epsilon A r^2}{8\mu\tau^2}, \quad (22)$$

where the notation follows Eq. (4). Introducing  $R_{loc}$  redistributes the replenishment flows: the flow from the left branch decreases while that from the right branch increases by an equal amount, so that the total flow still matches the evaporative flux. This implies that a greater fraction of the evaporated water is extracted from the pocket. This redistribution is favorable for the buildup of  $\Delta z_d$ : flow from the left vertical section comes directly from the sea and does not alter the water level in the salt-disposal device. In contrast, flow from the pocket lowers its water level and the buildup of  $\Delta z_d$  is accelerated.

To confirm this principle, the equivalent hydraulic circuit is analyzed (see Fig. D.1 in Appendix D), consistent with the experimental setup described in Section 2.4. In this configuration,  $R_{H,right}$  depends on  $\Delta z_d$  as given in Eq. (13). Since the circuit is interrupted at the location corresponding to  $R_{add}$ , this resistance tends to  $+\infty$ , so that  $R_{add} \gg R_{\alpha\beta,th}$ . The analysis is performed under the condition  $\Delta z_d \ll L$ .

The added localized resistance  $R_{loc}$  increases  $\Delta p_{\alpha\beta,th}$  and hence the steady-state hydraulic head difference  $\Delta z_{d,eq}$  in Eq. (14), giving:

$$\Delta z_{d,eq}^* \approx \frac{4\mu}{\rho^2 g (h_{gl}(T) - c_{p,w}T)} \left(\frac{\tau L}{r}\right)^2 \left(1 + 2\frac{H}{L} + 2\frac{\Delta L}{L}\right) \frac{\eta q_{sun}}{\epsilon s}. \quad (23)$$

The steady-state relative gain in hydraulic head is then:

$$G_{eq} = \frac{\Delta z_{d,eq}^* - \Delta z_{d,eq}}{\Delta z_{d,eq}} = \frac{2\Delta L/L}{1 + 2H/L}. \quad (24)$$

Because the time constant  $\tau_{ch}$  depends on  $R_{\alpha\beta,th}$  (Eq. (18)), the modification also affects system dynamics. In the new configuration,

$$\tau_{ch}^* \approx \frac{8\mu}{\rho g} \left(\frac{\tau L}{r}\right)^2 \left(1 + 2\frac{H}{L} + \frac{\Delta L}{L}\right) \frac{S_d}{\epsilon s B L}, \quad (25)$$

and the relative variation is

$$\frac{\tau_{ch}^* - \tau_{ch}}{\tau_{ch}} = \frac{\Delta L/L}{1 + 2H/L}. \quad (26)$$

Eq. (26) shows that the relative increase in  $\tau_{ch}$  scales linearly with  $\Delta L/L$ . In contrast, the relative gain in steady-state hydraulic head difference  $\Delta z_{d,eq}$  increases proportionally to  $2\Delta L/L$ , twice as much. Thus, the topological modification improves both steady-state and transient (early-time dynamics) performance. This becomes evident when analyzing the linear regime, valid for  $t \ll \tau_{ch}$ , in which the hydraulic head difference evolves approximately as  $\Delta z_d(t) \approx (\Delta z_{d,eq}/\tau_{ch}) t$ . In this limit,  $\Delta z_d^*(t)$  for the modified configuration becomes:

$$\Delta z_d^*(t) \approx \frac{\eta q_{sun}}{2\rho (h_{gl}(T) - c_{p,w}T)} \frac{S_d}{B L} \frac{1 + 2\frac{H}{L} + 2\frac{\Delta L}{L}}{1 + 2\frac{H}{L} + \frac{\Delta L}{L}} t. \quad (27)$$

The relative gain  $G_{lin}$  in hydraulic head difference due to the added localized resistance in the linear regime is:

$$G_{lin} = \frac{\Delta z_d^*(t) - \Delta z_d(t)}{\Delta z_d(t)} = 1 - \frac{1 + 2H/L}{1 + 2H/L + \Delta L/L}. \quad (28)$$

Figs. 7a and 7b show the relative gains  $G_{eq}$  and  $G_{lin}$ , expressed as percentages, as functions of  $\Delta L/L$  and  $H/L$ . In both cases, the gains increase monotonically with the dimensionless parameter  $\Delta L/L$ , independently of  $H/L$ . At steady-state, the relative change grows proportionally to  $2\Delta L/L$ , reaching values up to 2000% within the considered parameter range, i.e., up to twenty times the baseline value of  $\Delta z_{d,eq}$ . In the linear regime, which includes the early transient, the relative gain follows Eq. (28), approaching 90% for large  $\Delta L/L$ . This value represents the theoretical limit where nearly all evaporated water is supplied from the salt-disposal pocket. Conversely, increasing  $H/L$  has a monotonically negative effect on both gains, with  $G_{eq}$  being more sensitive than  $G_{lin}$ . As a result, the topological modification based on  $R_{loc}$  is more effective in systems characterized by low  $H/L$  ratios.

The larger value of  $G_{eq}$  compared to  $G_{lin}$  is physically consistent. While  $G_{lin}$  reflects the instantaneous enhancement in pocket-supplied flow during early transients (linear regime),  $G_{eq}$  incorporates cumulative effects over the entire operating period. In particular,  $G_{eq}$  is strongly influenced by the increase in  $\tau_{ch}$  (see Eq. (26)), which implies a longer time available for water withdrawal from the salt-disposal pocket during operation. However, excessively large increases in  $\tau_{ch}$  do not always translate into practical benefits, particularly when the baseline  $\tau_{ch}$  is already comparable to or larger than the device's operating period. In such cases, further extending the time constant does not lead to significant gains, since the additional absorption time cannot be fully exploited within the available operational window. The key insight from these plots is that the proposed topological modification yields a consistent and monotonic enhancement of  $\Delta z_d$  across all timescales, not only at steady state. Since siphon performance directly benefits from increased hydraulic gradients, this strategy provides a scalable way to further boost salt-rejection capability.

#### 4. Conclusions

This study demonstrates the feasibility and effectiveness of a fully passive, siphon-based mechanism for salt removal from the porous evaporator in solar-driven distillation devices. In this work, "fully passive" refers to the autonomous operation of the siphon-driven flushing mechanism responsible for evaporator regeneration, while downstream brine handling is treated as a decoupled, system-level design aspect. The novelty of this study lies in the autonomous generation of the hydraulic head required to trigger siphon flushing, rather than in the siphon mechanism per se. The system autonomously generates the hydraulic head required to activate siphon-driven rinsing cycles by coupling evaporation-induced mass loss with hydraulic equilibrium, enabling continuous brine flushing of the evaporator without external energy or manual intervention.

The analytical model, developed through the electric-hydraulic analogy, accurately captures both the transient and steady-state evolution of the hydraulic head difference  $\Delta z_d$  and the rinse number  $n_R$ . Experimental validation under controlled conditions confirms the predictive capability of the model: the device reliably develops measurable hydraulic heads and performs multiple rinsing cycles under typical solar irradiation. These findings directly address one of the primary limitations of passive distillation and desalination systems – salt accumulation – which hinders long-term stability and scalability.

Compared to diffusion-limited salt removal, the siphon mechanism achieves an order-of-magnitude faster regeneration, reducing near-saturated salinity to seawater levels within three hours. This confirms that passive hydraulic flushing is not only feasible but substantially more effective than diffusion for salt management. The scalability analysis further demonstrates that the proposed mechanism remains effective at meter-scale evaporator lengths. Representative numerical case studies show that 1-meter-long devices can safely operate below both dry-out and siphon-regeneration limits, while achieving rinse numbers exceeding unity under realistic solar irradiation. The geometric flexibility of the disposal pocket allows substantial salt dilution without compromising hydraulic head generation, ensuring operational stability over extended periods. Therefore, no intrinsic hydraulic limitation prevents scaling the concept to practical device sizes.

Despite the promising results, certain limitations remain. Proof-of-concept-experiments were conducted under controlled conditions. Nevertheless, because hydraulic head buildup depends on the time-integrated evaporative flux rather than on instantaneous irradiance, moderate temporal fluctuations in solar input are expected to primarily affect the timing and frequency of siphon activation rather than the feasibility of the flushing mechanism. Real-world deployments will need to account for fluctuating solar input, variable seawater composition, biofouling, and long-term material stability. Additionally, while the system effectively isolates salt in a disposal compartment, through the

fully passive operation of the siphon-based flushing mechanism, active or semi-passive removal mechanisms have yet to be integrated. By periodically and completely regenerating the evaporator, the siphon-driven flushing mechanism inherently suppresses salt crystallization within the porous matrix, helping preserve porosity and hydraulic resistance over time. While the present model assumes constant porosity, this assumption is justified for the operating regime targeted here and will be relaxed in future studies addressing long-term exposure to high salinity and fouling. Future designs should explore passive ejection strategies – such as overflow channels, one-way valves, or density-driven expulsion – to support continuous, maintenance-free operation. Addressing these challenges is essential for scaling the concept toward field-deployable distillation/desalination solutions. Alternatively, in a zero-liquid-discharge perspective, the concentrated brine collected in the disposal pocket could be periodically harvested for salt recovery, turning waste into a potentially valuable resource.

In summary, the proposed concept offers a scalable strategy compatible with meter-scale evaporators for salt management in evaporation-based desalination, capable of drastically reducing maintenance requirements. By overcoming diffusion limits and operating entirely without external power or control, it paves the way for robust, off-grid freshwater production in resource-limited settings. Beyond desalination, the same principle could be extended to other evaporation-driven processes where autonomous liquid regulation and solute management are required.

#### CRedit authorship contribution statement

**Roberto Raffaele Meo:** Writing – review & editing, Writing – original draft, Visualization, Validation, Methodology, Investigation, Formal analysis, Data curation, Conceptualization. **Stefan Morosanu:** Writing – original draft, Visualization, Validation, Methodology, Investigation, Formal analysis, Data curation. **Matteo Morciano:** Writing – review & editing, Validation, Supervision, Resources, Methodology, Investigation, Funding acquisition, Formal analysis, Conceptualization. **Matteo Fasano:** Writing – review & editing, Validation, Supervision, Resources, Methodology, Investigation, Funding acquisition, Formal analysis, Conceptualization.

#### Declaration of competing interest

The authors declare that they have no known competing financial interests or personal relationships that could have appeared to influence the work reported in this paper.

#### Acknowledgments

This work was funded by the European Union Horizon Europe Research and Innovation Program under grant agreement number 101091915 (acronym “MELODIZER”). Views and opinions expressed are however those of the author(s) only and do not necessarily reflect those of the European Union or the European Health and Digital Executive Agency (HADEA). Neither the European Union nor the granting authority can be held responsible for them. This publication is also part of the project PNRR-NGEU which has received funding from the MUR, Italy – DM 117/2023. The authors acknowledge Pietro Asinari, Eliodoro Chiavazzo and Luca Bergamasco for constructive discussions.

#### Appendix A. Hydraulic model

The electric–hydraulic analogy is used as the foundational framework to model fluid dynamics in the siphon-based salt removal device proposed in this work. This approach allowed us to conceptualize and quantify the viscous losses within the porous medium, which plays a critical role in the capillary water flow driven by solar-induced evaporation.

Viscous losses within the porous medium were modeled through its permeability, estimated via the Kozeny-Carman correlation (Nishiyama and Yokoyama, 2017). The permeability  $K$  of the porous medium is given by:

$$K = \frac{\epsilon r^2}{\gamma \tau^2}, \quad (\text{A.1})$$

where  $\epsilon$  is the porosity of the porous medium, defined as the ratio of the void volume to the total volume of the medium,  $r$  is the mean radius of the pores,  $\gamma$  is a parameter that depends on the pore shape and geometry, and  $\tau$  is the tortuosity of the porous medium, which accounts for the discrepancy between the actual mean flow path length and the thickness of the porous medium. For circular pores, as those assumed in this study,  $\gamma = 8$  (Nishiyama and Yokoyama, 2017). The tortuosity  $\tau$  is evaluated using the Mackie-Meares equation  $\tau = \frac{(2-\epsilon)^2}{\epsilon}$ , which provides a robust means of quantifying how the porosity affects the flow path's complexity and, consequently, the effective transport properties of the medium.

The pressure drop  $\Delta p$  across the porous medium is then given by (Meo and Morciano, 2022):

$$\Delta p = \frac{\epsilon \mu}{K} L v, \quad (\text{A.2})$$

where  $\mu$  is the dynamic viscosity,  $L$  is the length of the porous medium, and  $v$  is the flow velocity through the pores. Considering the definition of permeability  $K$  in Eq. (1) and defining the velocity  $v$  as the ratio of the flow rate  $Q$  to the effective cross-sectional area  $\epsilon A$  of the porous medium, the pressure drop becomes:

$$\Delta p = \frac{8 \mu \tau^2}{\epsilon A r^2} L Q. \quad (\text{A.3})$$

Starting from the hydraulic analogy  $\Delta p = R_{hydr} Q$ , which relates the pressure drop  $\Delta p$  across a flow path to the volumetric flow rate  $Q$  through the hydraulic resistance  $R_{hydr}$ , the hydraulic resistance of the porous medium can be expressed as:

$$R_{hydr} = \frac{8 \mu \tau^2}{\epsilon A r^2} L. \quad (\text{A.4})$$

The hydraulic resistance  $R_{hydr}$  encapsulates the influence of the porous medium's structural and material properties on the flow resistance, serving as a critical parameter for evaluating the device's efficiency.

The schematic of the device shown in Fig. 1 consists of three main sections of the porous medium: the left vertical section, the right vertical section, and the central horizontal evaporator. Each of these sections is characterized by a hydraulic resistance due to their porous nature. For the left vertical section, the hydraulic resistance is expressed as:

$$R_{H,left} = \frac{8 \mu \tau^2}{\epsilon A r^2} H, \quad (\text{A.5})$$

where  $H$  is the height of the section, and  $r$  represents the pore radius. The right vertical section, on the other hand, consists of two segments in series. The first segment (that is an additional resistance), shorter and located at depth in direct contact with the sea, has the following hydraulic resistance:

$$R_{add} = \frac{8 \mu \tau^2}{\epsilon A r_{add}^2} H_{add}, \quad (\text{A.6})$$

where  $H_{add}$  and  $r_{add}$  are the height and equivalent pore radius of this specific segment, respectively. To characterize the second segment, it is necessary to introduce the quantity  $z_O$ , which represents the depth at which the connection to the salt disposal device is established. This is defined as:

$$z_O = z_{sea} - H_{add}, \quad (\text{A.7})$$

where  $z_{sea}$  represents the depth of the interface between the first segment (i.e., the additional resistance) and the sea. The hydraulic

resistance of the second segment of the right vertical section can then be expressed as:

$$R_{H,right} = \frac{8\mu\tau^2}{\epsilon Ar^2}(H + z_O). \quad (\text{A.8})$$

The central horizontal evaporator is assumed to undergo distributed evaporation. To capture this behavior, it is initially modeled as a continuum of infinitesimal hydraulic resistances arranged in series. Each infinitesimal resistance is defined by the following expression:

$$dR_e = \frac{8\mu\tau^2}{\epsilon Ar^2} dx, \quad (\text{A.9})$$

where  $dx$  represents an infinitesimal length of the evaporator.

In addition to hydraulic resistances, the circuit representation of the hydraulic model must also account for elevation effects and fluid storage within the salt-disposal device. A fixed elevation difference can be modeled as a voltage generator. According to Stevin's law, which relates pressure differences to fluid properties and height variations, the following expression is obtained:

$$\Delta p = \rho g \Delta z, \quad (\text{A.10})$$

where  $\rho$  is the fluid density,  $g$  the gravitational acceleration, and  $\Delta z$  the elevation difference. In contrast, the elevation  $z_d(t)$  of the water free surface in the salt-disposal device (as indicated in Fig. 1) evolves in time, before reaching steady state, and is therefore modeled as a capacitor. The corresponding pressure difference between the static pressure intake and the free surface in the salt-disposal device is again given by Stevin's law:

$$\Delta p(t) = \rho g z_d(t), \quad (\text{A.11})$$

Throughout the analysis, dynamic pressure contributions  $\Delta p_d$  are assumed to be negligible compared to viscous pressure drops  $\Delta p_v$ . This assumption is validated in the following Appendix B: Dynamic pressure assessment, where  $\Delta p_d$  and  $\Delta p_v$  are explicitly compared for each section of the device.

## Appendix B. Dynamic pressure assessment

For the left vertical section in Fig. 1, let  $\dot{z}$  represent the flow velocity within the porous medium section. The dynamic pressure is given by:

$$\Delta p_d = \frac{1}{2} \rho \dot{z}^2, \quad (\text{B.1})$$

while the viscous pressure drop is expressed as:

$$\Delta p_v = \frac{8\mu\tau^2}{r^2} \dot{z}. \quad (\text{B.2})$$

Considering water as fluid, the ratio between the two contributions becomes:

$$\frac{\Delta p_d}{\Delta p_v} \simeq 10^6 \frac{r^2}{H} \dot{z} \quad (\text{B.3})$$

Given that  $r$  is on the order of  $10^{-6}$  m for typical porous medium employed in passive distillation applications,  $H$  is in the range of mm, and  $\dot{z}$  is much smaller than 1 m/s, it follows that  $\frac{\Delta p_d}{\Delta p_v} \ll 1$ . This confirms the validity of the assumption that the dynamic pressure is negligible compared to the viscous pressure drop in this section.

For the right vertical section, a similar analysis is performed. For simplicity, only one segment is considered to calculate the viscous losses, neglecting  $R_{add}$ , which is a conservative assumption. In this case, the ratio becomes:

$$\frac{\Delta p_d}{\Delta p_v} \simeq 10^6 \frac{r^2}{H + z_O} \dot{z}. \quad (\text{B.4})$$

Again, using the same typical values for  $r$ ,  $H$ ,  $z_O$ , and  $\dot{z}$ , the ratio  $\frac{\Delta p_d}{\Delta p_v}$  is found to be  $\ll 1$ , demonstrating that the dynamic pressure is negligible

compared to the viscous pressure drop for the right vertical section as well.

For the horizontal section, the analysis must be conducted in infinitesimal terms. Let  $\dot{x}$  denote the flow velocity in the section. The infinitesimal variation of the dynamic pressure, obtained by differentiation, is expressed as:

$$d\Delta p_d = \rho \dot{x} d\dot{x}. \quad (\text{B.5})$$

The viscous pressure drop is given by:

$$d\Delta p_v = \frac{8\mu\tau^2}{r^2} \dot{x} dx. \quad (\text{B.6})$$

The ratio between the infinitesimal contributions is then:

$$\frac{d\Delta p_d}{d\Delta p_v} = \frac{\rho r^2}{8\mu\tau^2} \frac{d\dot{x}}{dx}. \quad (\text{B.7})$$

$\frac{d\dot{x}}{dx}$  can be derived from the expression that describes the evaporator flow velocity. Under the assumption of steady-state isothermal conditions, the flow velocity is given by the following relation (Meo and Morciano, 2022):

$$\dot{x}(x) = \dot{x}_0 - \frac{\eta \frac{q_{sun}}{s} x}{\epsilon \rho (h_{gl}(T) - c_{p,w}T)}, \quad (\text{B.8})$$

where  $\dot{x}(x)$  represents the flow velocity as a function of the position  $x$ , and  $\dot{x}_0$  denotes the inlet flow velocity of the evaporator. The parameters  $\eta$ ,  $q_{sun}$  and  $s$  correspond to solar absorption efficiency, solar irradiance, and evaporator thickness, respectively. Additionally,  $\rho$  is water density,  $\epsilon$  is the porosity of the porous medium,  $h_{gl}$  latent heat of vaporization,  $c_{p,w}$  specific heat capacity of water, and  $T$  refers to the temperature of the porous medium. Hence:

$$\frac{d\dot{x}}{dx} = - \frac{\eta \frac{q_{sun}}{s}}{\epsilon \rho (h_{gl}(T) - c_{p,w}T)}. \quad (\text{B.9})$$

Substituting typical values for the parameters involved, the ratio simplifies to:

$$\frac{d\Delta p_d}{d\Delta p_v} \simeq -10^{-5} r^2 \frac{\eta q_{sun}}{s}. \quad (\text{B.10})$$

Given that  $r$  is on the order of  $10^{-6}$  m,  $\eta q_{sun}$  is approximately 1000 W/m<sup>2</sup>, and  $s$  is on the order of a few mm, it follows that, even in the horizontal section, for each infinitesimal segment,  $\frac{\Delta p_d}{\Delta p_v} \ll 1$ . This confirms that the dynamic pressure contribution is negligible in every infinitesimal segment of the horizontal section.

## Appendix C. Thevenin equivalent model

Fig. 2 presents the hydraulic schematic of the passive solar distillation system, derived using the electric-hydraulic analogy and assuming that dynamic pressure is negligible relative to other pressure contributions. The objective is to determine the Thevenin equivalent circuit and the corresponding pressure difference  $\Delta p_{\alpha\beta,th}$  between the two terminals  $\alpha$  and  $\beta$ , which bound the salt-disposal branch (see Fig. C.1). In the following derivation, the vertical flow rate  $Q_v$  and the evaporative flow rate  $Q_e$  are defined for the open-circuit configuration shown in Fig. C.1, where the salt-disposal branch is disconnected and the entire flow passes through the left leg. The same notation is used in Fig. 2 for consistency, although the corresponding values differ since that configuration represents the complete, closed circuit.

To obtain  $\Delta p_{\alpha\beta,th}$ , the pressure drops along the main porous sections of the system are evaluated individually. First, the pressure drop in the left vertical section is evaluated, which is associated to the corresponding flow rate  $Q_v$ . This flow rate is obtained as the integral of all infinitesimal contributions associated with the evaporative flow rate in the central section. Under the assumption of steady-state isothermal

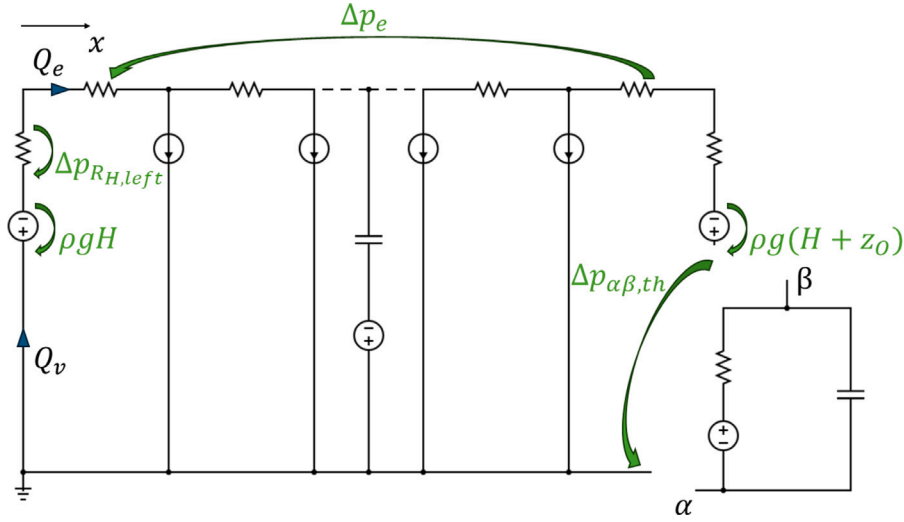


Fig. C.1. Procedure for evaluating the Thevenin equivalent pressure and resistance with respect to terminals  $\alpha$  and  $\beta$ . The equivalent pressure is computed under open-circuit conditions; the equivalent resistance is obtained by suppressing independent sources and measuring the resulting impedance.

conditions, it is possible to demonstrate that (Meo and Morciano, 2022):

$$d\dot{x} = -\frac{\eta_{local} \frac{q_{sun}}{s}}{\epsilon \rho (h_{gl}(T) - c_{p,w}T)} dx, \quad (C.1)$$

where  $\dot{x}$  represents the flow velocity through the pores in the horizontal evaporator. The parameters  $\eta_{local}$ ,  $q_{sun}$  and  $s$  correspond to effective local evaporation efficiency, solar irradiance, and evaporator thickness, respectively. Additionally,  $\rho$  is water density,  $\epsilon$  is the porosity of the porous medium,  $h_{gl}$  latent heat of vaporization,  $c_{p,w}$  specific heat capacity of water, and  $T$  refers to the temperature of the porous medium. Here,  $\eta_{local}(x)$  accounts not only for heat losses to the ambient, but also for the fraction of absorbed solar energy that is locally converted to sensible heating of the liquid/porous medium rather than driving evaporation. This is particularly relevant near the evaporator inlet, where entering seawater is warmed up in a short region and the temperature field may not be uniform. As shown in our previous work (Meo and Morciano, 2022), the resulting temperature gradients remain limited under typical operating conditions, supporting the use of the present formulation. Hence, the infinitesimal contributions to the evaporative flow rate are expressed as:

$$dQ_e = \frac{\eta_{local} \frac{q_{sun}}{s} A}{\rho (h_{gl}(T) - c_{p,w}T)} dx \quad (C.2)$$

where  $A$  is the cross-section of the porous medium. The flow rate in the left vertical section can be thus derived as

$$Q_v = \int_0^L dQ_e = \frac{\eta \frac{q_{sun}}{s}}{\rho (h_{gl}(T) - c_{p,w}T)} L A, \quad (C.3)$$

with the corresponding pressure drop

$$\Delta p_{R_{H,left}} = R_{H,left} Q_v = \frac{8\mu\tau^2}{\epsilon\rho r^2} \frac{\eta \frac{q_{sun}}{s}}{h_{gl}(T) - c_{p,w}T} LH. \quad (C.4)$$

$\eta$  is the effective global efficiency, i.e. the ratio between the total vapor flow rate produced by the real evaporator and that of an ideal evaporator converting all the absorbed heat into vapor. Second, the pressure drop within the horizontal evaporator is evaluated. Since the evaporator is characterized by distributed evaporation, the contributions from individual segments must be integrated. Specifically, the flow rate as a function of the distance  $x$  is expressed as:

$$Q_e = Q_v - \int_0^x dQ_e = \frac{\eta_{local}^* \frac{q_{sun}}{s}}{\rho (h_{gl}(T) - c_{p,w}T)} A(L - x), \quad (C.5)$$

Here,  $\eta_{local}^*$  is an effective correction of  $\eta_{local}$  that accounts for its spatial variability along the evaporator, i.e. it represents the equivalent coefficient resulting from the integration of  $\eta_{local}(x)$  in the definition of  $Q_e(x)$ . The total pressure drop across the horizontal evaporator is given by

$$\Delta p_e = \int_0^L Q_e dR_e = \frac{8\mu\tau^2}{\epsilon\rho r^2} \frac{\eta^* \frac{q_{sun}}{s}}{h_{gl}(T) - c_{p,w}T} \frac{L^2}{2}. \quad (C.6)$$

$\eta^*$  is a hydraulic correction of  $\eta$ , since it accounts for the impact of a spatially non-uniform evaporation profile on viscous dissipation. Third, the hydrostatic contributions in the two vertical branches are accounted for (see Fig. C.1). Using Stevin's law ( $\Delta p = \rho g \Delta z$ ) and adopting the sign convention of Kirchhoff's second law along the loop from  $\alpha$  to  $\beta$ : (i) in the left branch the path rises by a height  $H$  from the reference free surface at  $p_{atm}$  to the horizontal evaporator plane, hence the contribution is  $+\rho g H$ ; (ii) in the right branch, the circuit is open at  $\alpha-\beta$  when evaluating the Thevenin pressure, so no flow passes through the porous leg and the viscous drop across  $R_{H,right}$  is zero. Only the elevation change between  $\alpha$  (free surface at  $p_{atm}$ ) and  $\beta$  (node just upstream of the static-pressure tap  $O$  at depth  $z_O$ ) contributes, giving a hydrostatic drop  $\rho g(H + z_O)$  that enters with a negative sign. Collecting the hydrostatic terms with the viscous drops in the left vertical section and in the horizontal evaporator, the Thevenin pressure  $\Delta p_{\alpha\beta,th}$  can be eventually determined:

$$\Delta p_{\alpha\beta,th} = \Delta p_e + \Delta p_{R_{H,left}} + \rho g H - \rho g(H + z_O), \quad (C.7)$$

which simplifies to

$$\Delta p_{\alpha\beta,th} = \frac{8\mu\tau^2}{\epsilon\rho r^2} \frac{\eta \frac{q_{sun}}{s}}{h_{gl}(T) - c_{p,w}T} L \left( \frac{L}{2} + \frac{\eta^*}{\eta} H \right) - \rho g z_O. \quad (C.8)$$

The expression of  $\Delta p_{\alpha\beta,th}$  highlights how non-uniform evaporation affects not only the global evaporation efficiency  $\eta$  but also viscous dissipation, since lower evaporation implies lower flow velocities and therefore reduced viscous losses compared to the ideal case. This effect is embedded through the factor  $\eta^*/\eta$  multiplying  $H$ . As shown in our previous work (Meo and Morciano, 2022), evaporation-rate gradients induced by spatial temperature variations are generally negligible and remain confined to a short inlet warm-up region, thus having a limited impact. Hence, to preserve a compact analytical model, we reasonably adopt  $\eta^* \approx \eta$ . Next, the Thevenin equivalent resistance between  $\alpha$  and  $\beta$ ,  $R_{\alpha\beta,th}$ , is computed. First, the resistance of the evaporator is determined from Eq. (A.9) as:

$$R_e = \int_0^L dR_e = \frac{8\mu\tau^2}{\epsilon A r^2} L. \quad (C.9)$$

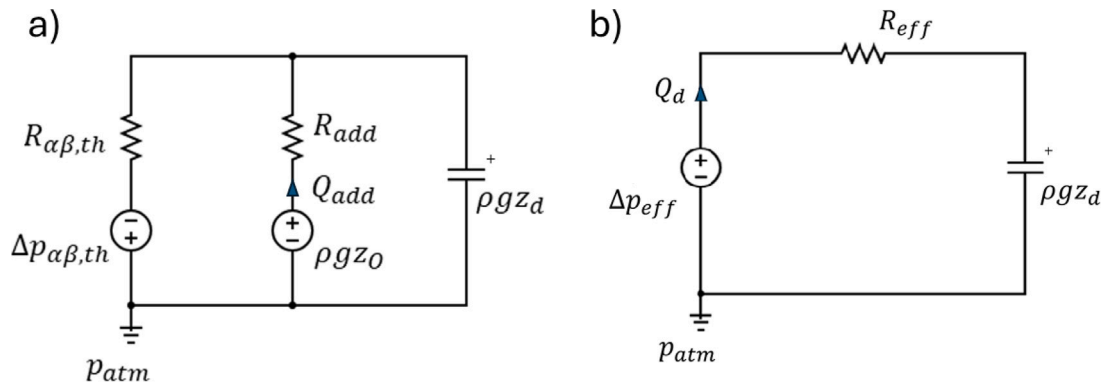


**Fig. C.2.** (a) Simplified equivalent circuit representation of the distillation device. This schematic results from the Thevenin equivalent transformation with respect to terminals  $\alpha$  and  $\beta$ , reducing the complexity of the original network. The simplified model retains the key electric–hydraulic analog parameters while providing a more compact and computationally efficient representation for analysis. (b) Thevenin reduction at the capacitor terminals yields an elementary RC equivalent with an effective pressure source. The source  $\Delta p_{eff}$  (referenced to  $p_{atm}$ ) is in series with the hydraulic resistance  $R_{eff}$  and a hydraulic capacitor representing the hydrostatic head  $\rho g z_d$ . The loop flow  $Q_d$  equals  $S_d \dot{z}_d$  and represents the volumetric flow through the salt-disposal device cross-section  $S_d$  (assumed uniform).

By short-circuiting the pressure generators and opening the circuit at the current generators,  $R_{\alpha\beta,th}$  is found as the series combination of three hydraulic resistances:

$$R_{\alpha\beta,th} = R_{H,left} + R_e + R_{H,right}, \quad (C.10)$$

which, considering Eqs. (A.5), (A.8) and (C.9), results in

$$R_{\alpha\beta,th} = \frac{8\mu\tau^2}{\epsilon A r^2} (2H + L + z_O). \quad (C.11)$$

In the simplified circuit, under steady-state conditions (where steady-state quantities are denoted by the subscript “eq”), as the capacitor which generates  $\rho g z_d$  behaves as an open circuit, the flow rate passing through the additional resistance  $R_{add}$  is equal to that passing through the Thevenin equivalent resistance  $R_{\alpha\beta,th}$  and can be determined using Ohm’s law:

$$Q_{add,eq} = \frac{\Delta p_{\alpha\beta,th} + \rho g z_O}{R_{\alpha\beta,th} + R_{add}}. \quad (C.12)$$

Applying Kirchhoff’s second law to the loop containing the capacitor yields

$$\rho g z_{d,eq} = \rho g z_O - R_{add} Q_{add,eq}. \quad (C.13)$$

Combining Eqs. (C.12) and (C.13) yields:

$$z_O - z_{d,eq} = \frac{R_{add}}{\rho g} \frac{\Delta p_{\alpha\beta,th} + \rho g z_O}{R_{\alpha\beta,th} + R_{add}}. \quad (C.14)$$

Defining the steady-state hydraulic head difference in the capacitor as  $\Delta z_{d,eq} = z_O - z_{d,eq}$ , and recalling Eqs. (A.6), (C.7) and (C.11), the following expression is derived

$$\Delta z_{d,eq} = \frac{4\mu\tau^2}{\epsilon g \rho^2 r^2} \frac{\eta \frac{q_{sun}}{s} L}{h_{gl}(T) - c_{p,w} T} \frac{2H + L}{1 + \frac{r_{add}^2}{r^2} \frac{2H + L + z_O}{H_{add}}}. \quad (C.15)$$

Assuming that the pore radius of the additional resistance is several orders of magnitude smaller than the pore radius of the remaining porous material, i.e.,  $r_{add} \ll r$ , the simplified expression becomes

$$\Delta z_{d,eq} \approx \frac{4\mu}{\rho^2 g (h_{gl}(T) - c_{p,w} T)} \left( \frac{\tau L}{r} \right)^2 \left( 1 + 2 \frac{H}{L} \right) \frac{\eta q_{sun}}{\epsilon s}. \quad (C.16)$$

To evaluate the temporal evolution of the water level in the capacitor (i.e., the salt-disposal pocket), in addition to the steady-state hydraulic head difference  $\Delta z_{d,eq}$ ; it is essential to assess the characteristic time constant governing water accumulation and release.

Applying Thevenin’s theorem at the capacitor terminals, the circuit in Fig. C.2a reduces to an elementary RC (resistor–capacitor) system driven by an effective pressure (voltage) source, as shown in Fig. C.2b. Specifically, it consists of three series elements: an effective pressure source  $\Delta p_{eff}$ , a lumped resistance  $R_{eff}$ , and a capacitor representing the hydrostatic pressure  $\rho g z_d$ .

This equivalent circuit can be interpreted as a pump that exerts  $\Delta p_{eff}$  in series with  $R_{eff}$ . At rest, in the absence of evaporation,  $\Delta p_{eff} = \rho g z_O$  and  $z_d = z_O$ , hence  $\Delta z_d = 0$ . During daytime, evaporation modulates the pump and reduces  $\Delta p_{eff}$ . This decrease lowers  $z_d$  relative to its rest value  $z_O$ , thereby creating a positive hydraulic head difference  $\Delta z_d = z_O - z_d > 0$  as water is extracted from the pocket (piezometer-like behavior). At night, when evaporation ceases,  $\Delta p_{eff}$  rises back to  $\rho g z_O$  and  $z_d$  relaxes to  $z_O$ , corresponding to pocket refilling and the gradual decay of  $\Delta z_d$ . While  $\Delta p_{eff}$  varies between daytime and nighttime due to changing operating conditions, specifically the presence or absence of evaporative flows,  $R_{eff}$  depends solely on the circuit topology and remains unchanged. The equivalent resistance  $R_{eff}$  is given by:

$$R_{eff} = \left( \frac{1}{R_{\alpha\beta,th}} + \frac{1}{R_{add}} \right)^{-1}. \quad (C.17)$$

Assuming again  $r_{add} \ll r$  thus  $R_{add} \gg R_{\alpha\beta,th}$ , Eq. (C.17) becomes

$$R_{eff} \approx R_{\alpha\beta,th}. \quad (C.18)$$

A pressure balance (Kirchhoff’s second law) on the Thevenin-reduced RC loop indicated in Fig. C.2b gives:

$$\Delta p_{eff} = \rho g z_d + R_{eff} Q_d, \quad (C.19)$$

being  $Q_d = S_d \dot{z}_d$  the volumetric flow through the cross-section  $S_d$  of the device (assumed uniform). Since the circuit elements are in series, the same  $Q_d$  traverses all of them. Eq. (C.19) can be then reshaped as

$$\dot{z}_d + \frac{\rho g}{R_{eff} S_d} z_d = \frac{\Delta p_{eff}}{R_{eff} S_d}. \quad (C.20)$$

Eq. (C.20) is a first-order differential equation describing the transient evolution of  $z_d$ , which also governs  $\Delta z_d$ , since  $\Delta z_d(t) = z_O - z_d(t)$ .

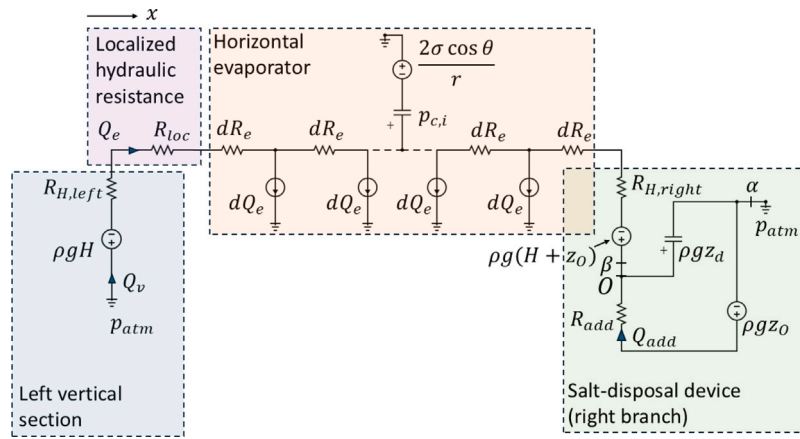


**Fig. D.1.** Equivalent circuit representation of the passive siphon-driven distillation device including the localized hydraulic resistance  $R_{loc}$  on the left branch. The extra resistance, placed in series with the original left vertical section, redistributes the flow drawn by the evaporator, increases the Thevenin pressure at the salt-disposal device, and ultimately boosts the steady hydraulic head difference  $\Delta z_{d,eq}$ . Circuit symbols and parameters follow the same notation as in Fig. 2.

From Eqs. (C.11) and (C.18), the corresponding characteristic time constant is:

$$\tau_{ch} = \frac{R_{eff} \cdot S_d}{\rho g} = \frac{8\mu}{\rho g} \left( \frac{\tau L}{r} \right)^2 \left( 1 + 2 \frac{H}{L} + \frac{z_O}{L} \right) \frac{S_d}{\epsilon s B L}. \quad (C.21)$$

Solving Eq. (C.20) yields the temporal evolution of the hydraulic head difference:

$$\Delta z_d(t) = \Delta z_{d,eq} \left( 1 - e^{-\frac{t}{\tau_{ch}}} \right). \quad (C.22)$$

Considering the magnitude of the involved parameters,  $\tau_{ch}$  can be on the order of hundreds of hours, which is significantly greater than the operational time  $t$  of the solar distiller, typically on the order of few hours. Under the assumption  $\frac{t}{\tau_{ch}} \rightarrow 0$ , Eq. (C.22) can be then linearized by Taylor expansion:

$$\Delta z_d(t) \approx \Delta z_{d,eq} \frac{t}{\tau_{ch}} = \frac{\eta q_{sun} \left( 1 + 2 \frac{H}{L} \right)}{2 \rho (h_{gl}(T) - c_{p,w} T) \left( 1 + 2 \frac{H}{L} + \frac{z_O}{L} \right) \frac{S_d}{BL}} t \quad (C.23)$$

To evaluate the performance of the spontaneous salt-removal device, the rinse number is defined as a dimensionless metric that quantifies how many times the effective evaporator volume ( $V_{ol_e}$ ) is replenished by the siphon-driven flow from the salt-disposal device ( $V_{ol_d}$ ):

$$n_R = \frac{V_{ol_d}}{V_{ol_e}} = \frac{\Delta z_d S_d}{\epsilon s B L}. \quad (C.24)$$

Moreover, considering Eq. (C.23), the number of complete rinsing events per operational time can be expressed as:

$$\frac{n_R}{t} = \frac{\eta q_{sun}}{2 \epsilon s \rho (h_{gl}(T) - c_{p,w} T)} \frac{1 + 2 \frac{H}{L}}{1 + 2 \frac{H}{L} + \frac{z_O}{L}}. \quad (C.25)$$

#### Appendix D. Equivalent circuit of the topological modification with localized hydraulic resistance $R_{loc}$

See Fig. D.1.

#### Appendix E. Nomenclature

| Symbol            | Description   | Unit                             |
|-------------------|---|----------------------------------|
| $g$               | Gravitational acceleration  | $\text{m s}^{-2}$                |
| $\mu$             | Water dynamic viscosity   | Pa s                             |
| $\rho$            | Water density   | $\text{kg m}^{-3}$               |
| $h_{gl}$          | Water latent heat of vaporization   | $\text{J kg}^{-1}$               |
| $c_{p,w}$         | Water specific heat capacity  | $\text{J kg}^{-1} \text{K}^{-1}$ |
| $q_{sun}$         | Solar irradiance  | $\text{W m}^{-2}$                |
| $\eta_{local}(x)$ | Local effective evaporation efficiency  | –                                |
| $\eta$            | Global effective evaporation efficiency   | –                                |
| $\eta^*$          | Hydraulic correction of $\eta$ accounting for pressure-drop distribution (viscous losses) | –                                |
| $T$               | Porous-medium temperature   | $^{\circ}\text{C}$               |
| $r$               | Characteristic pore radius of the porous evaporator                                       | m                                |
| $\epsilon$        | Porosity of the porous medium   | –                                |
| $\tau$            | Tortuosity of the porous medium   | –                                |
| $K$               | Permeability of the porous medium (Kozeny–Carman)   | $\text{m}^2$                     |
| $H$               | Height of the horizontal evaporator above sea level                                       | m                                |
| $L$               | Evaporator length (horizontal section)  | m                                |
| $B$               | Evaporator width  | m                                |
| $s$               | Evaporator thickness  | m                                |
| $A$               | Evaporator cross-sectional area, i.e., $A = Bs$   | $\text{m}^2$                     |
| $H_{add}$         | Length of the added high-resistance section   | m                                |
| $r_{add}$         | Pore radius of the added high-resistance section  | m                                |
| $S_d$             | Cross-sectional area of the salt disposal device  | $\text{m}^2$                     |
| $z_d$             | Free-surface elevation in the salt-disposal pocket  | m                                |
| $z_O$             | Depth of the connection point (tap $O$ ) between porous medium and disposal device        | m                                |

|                             |  |              |  |
|-----------------------------|--|--------------|--|
| $z_{sea}$                   | Depth of the interface between the additional resistance and the sea           | m            | Kuang, Y., Chen, C., He, S., Hitz, E.M., Wang, Y., Gan, W., Mi, R., Hu, L., 2019. A high-performance self-regenerating solar evaporator for continuous water desalination. <i>Adv. Mater.</i> 31 (23), 1900498.  |
| $\Delta z_d$                | Hydraulic head difference in the disposal device, $\Delta z_d = z_O - z_d$     | m            | Kumar, S., Kumar, M., Chowdhury, S., Rajpurohit, B., Randhawa, J., 2022. Environmental concerns and long-term solutions for solar-powered water desalination. <i>J. Cleaner Prod.</i> 131180.  |
| $\Delta z_{d,eq}$           | Steady-state hydraulic head difference   | m            | Lei, Z., Sun, X., Zhu, S., Dong, K., Liu, X., Wang, L., Zhang, X., Qu, L., Zhang, X., Su, Y., Cheng, H.-M., 2024. A portable and washable solar steam evaporator based on graphene and recycled gold for efficient point-of-use water purification. <i>Sci. China Mater.</i> 67 (11), 3700–3709.   |
| $Q$                         | Volumetric flow rate (generic)   | $m^3 s^{-1}$ | Li, W., Li, Z., Bertelsmann, K., Fan, D.E., 2019. Portable low-pressure solar steaming-collection unisystem with polypyrrole origamis. <i>Adv. Mater.</i> 31 (29), 1900720.  |
| $Q_v$                       | Volumetric flow rate in the left vertical section                              | $m^3 s^{-1}$ | Li, Z., Xing, Y., Fan, X., Lin, L., Meng, A., Li, Q., 2018. Rgo/protonated g-c3n4 hybrid membranes fabricated by photocatalytic reduction for the enhanced water desalination. <i>Desalination</i> 443, 130–136.   |
| $\dot{x}$                   | Local flow velocity through pores in the horizontal evaporator                 | $m s^{-1}$   | Liu, K.-K., Jiang, Q., Tadepalli, S., Raliya, R., Biswas, P., Naik, R.R., Singamaneni, S., 2017. Wood-graphene oxide composite for highly efficient solar steam generation and desalination. <i>ACS Appl. Mater. Interfaces</i> 9 (8), 7675–7681.  |
| $\Delta p$                  | Pressure difference (generic)  | Pa           | Mauter, M.S., Fiske, P.S., 2020. Desalination for a circular water economy. <i>Energy Env. Sci.</i> 13 (10), 3180–3184.  |
| $\Delta p_{\alpha\beta,th}$ | Thevenin equivalent pressure difference between terminals $\alpha$ and $\beta$ | Pa           | Mauter, M.S., Zucker, I., Perreault, F., Werber, J.R., Kim, J.-H., Elimelech, M., 2018. The role of nanotechnology in tackling global water challenges. <i>Nat. Sustain.</i> 1 (4), 166–175.   |
| $R_{hydr}$                  | Hydraulic resistance of a porous section (generic)                             | $Pa m^{-3}$  | Mekonnen, M.M., Hoekstra, A.Y., 2016. Four billion people facing severe water scarcity. <i>Sci. Adv.</i> 2 (2), e1500323.  |
| $R_{H,left}$                | Hydraulic resistance of the left vertical porous section                       | $Pa m^{-3}$  | Meo, R.R., Craveri, L., Bertozzi, E., Malaguti, M., Tiraferri, A., Morciano, M., Fasano, M., 2025. Systematic exploration of direct solar absorption potential to enhance direct contact membrane distillation. <i>Desalination</i> 606, 118740.   |
| $R_{H,right}$               | Hydraulic resistance of the right vertical porous section                      | $Pa m^{-3}$  | Meo, R.R., Morciano, M., 2022. Investigating the potentials and limitations of capillary-fed vapor generators: A heat and mass transfer study. <i>Int. Commun. Heat Mass Transfer</i> 137, 106309.   |
| $R_{add}$                   | Added hydraulic resistance of the high-resistance section connected to the sea | $Pa m^{-3}$  | Meo, R.R., Provenzano, M., Morciano, M., 2023. Investigating the solute concentration in capillary-fed vapor generators: A heat and mass transfer study. <i>Int. Commun. Heat Mass Transfer</i> 148, 106998. <a href="http://dx.doi.org/10.1016/j.icheatmasstransfer.2023.106998">http://dx.doi.org/10.1016/j.icheatmasstransfer.2023.106998</a> .   |
| $R_e$                       | Hydraulic resistance of the horizontal evaporator                              | $Pa m^{-3}$  | Nishiyama, N., Yokoyama, T., 2017. Permeability of porous media: Role of the critical pore size. <i>J. Geophys. Res.: Solid Earth</i> 122 (9), 6955–6971.  |
| $R_{\alpha\beta,th}$        | Thevenin equivalent resistance between terminals $\alpha$ and $\beta$          | $Pa m^{-3}$  | Sharon, H., Reddy, K., 2015. A review of solar energy driven desalination technologies. <i>Renew. Sustain. Energy Rev.</i> 41, 1080–1118.  |
| $\tau_{ch}$                 | Characteristic time constant for head build-up (RC time constant)              | s            | Stincone, G., Meo, R.R., Chiavazzo, E., Asinari, P., Fasano, M., Morciano, M., 2024. Optimizing the marangoni effect towards enhanced salt rejection in thermal passive desalination. <i>Desalination</i> 583, 117673.   |
| $n_R$                       | Rinse number, $n_R = Vol_d / Vol_e$  | –            | Wang, J., Li, Y., Deng, L., Wei, N., Weng, Y., Dong, S., Qi, D., Qiu, J., Chen, X., Wu, T., 2017. High-performance photothermal conversion of narrow-bandgap ti2o3 nanoparticles. <i>Adv. Mater.</i> 29 (3), 1603730.  |
| $L_{lim,siphon}$            | Limiting evaporator length for siphon flushing                                 | m            | Wang, Y., Wang, C., Song, X., Megarajan, S.K., Jiang, H., 2018. A facile nanocomposite strategy to fabricate a rgo-mwcnt photothermal layer for efficient water evaporation. <i>J. Mater. Chem. A</i> 6 (3), 963–971.  |
| $t_{tis}$                   | Disposal time (time for brine/salt discharge)                                  | s            | World Water Assessment Programme, 2016. The united nations world water development report.   |
| $t_{op}$                    | Operation (illumination) time  | s            | Xia, Y., Hou, Q., Jubaer, H., Li, Y., Kang, Y., Yuan, S., Liu, H., Woo, M.W., Zhang, L., Gao, L., Wang, H., Zhang, X., 2019. Spatially isolating salt crystallisation from water evaporation for continuous solar steam generation and salt harvesting. <i>Energy Env. Sci.</i> 12 (6), 1840–1847. <a href="http://dx.doi.org/10.1039/C9EE00692C">http://dx.doi.org/10.1039/C9EE00692C</a> . |

## Data availability

The data supporting this article are available on Zenodo: <https://doi.org/10.5281/zenodo.17422758>.

## References

- Angelis, P. De, Tuninetti, M., Bergamasco, L., Caliano, L., Asinari, P., Laio, F., Fasano, M., 2021. Data-driven appraisal of renewable energy potentials for sustainable freshwater production in africa. *Renew. Sustain. Energy Rev.* 149, 111414.
- Chen, Y., Yang, J., Zhu, L., Wang, S., Jia, X., Li, Y., Shao, D., Feng, L., Song, H., 2023. Marangoni-driven biomimetic salt secretion evaporator. *Desalination* 548, 116287.
- Chiavazzo, E., Morciano, M., Viglino, F., Fasano, M., Asinari, P., 2018. Passive solar high-yield seawater desalination by modular and low-cost distillation. *Nat. Sustain.* 1 (12), 763–772.
- Deka, N., Qari, M.M., Dash, S., 2025. Siphon-based scalable and salt-resistant multistage thermal desalination system. *Desalination* 593, 118200.
- Fan, X., Peng, Y., Lv, B., Yang, Y., You, Z., Song, C., Xu, Y., 2023. A siphon-based spatial evaporation device for efficient salt-free interfacial steam generation. *Desalination* 552, 116442.
- He, W., Huang, G., Markides, C., 2023. Synergies and potential of hybrid solar photovoltaic-thermal desalination technologies. *Desalination* 552, 116424.
- Huang, X., Yu, Y.-H., de Llergo, O.L., Marquez, S.M., Cheng, Z., 2017. Facile polypyrrole thin film coating on polypropylene membrane for efficient solar-driven interfacial water evaporation. *RSC Adv.* 7 (16), 9495–9499.
- Kelley, C.P., Mohtadi, S., Cane, M.A., Seager, R., Kushnir, Y., 2015. Climate change in the fertile crescent and implications of the recent syrian drought. *PNAS* 112 (11), 3241–3246.
- Xue, W., Zhao, Z., Zhao, G., Bi, H., Zhu, H., Wang, X., Qiu, J., 2024. Solar-driven salt-free deposition evaporation for simultaneous desalination and electricity generation based on tip-effect and siphon-effect. *J. Energy Chem.* 98, 364–373.
- Yang, Z., Li, D., Yang, K., Chen, L., Wang, J., Zhu, X., Chen, B., 2023. Optimized water supply in a solar evaporator for simultaneous freshwater production and salt recycle. *Environ. Sci. Technol.* 57 (35), 13047–13055.
- Yang, Y., Liu, C., Wang, J., Xu, G., Ren, T., 2023. Janus 3D graphene based evaporator with controllable wettability for highly efficient solar desalination. *Desalination* 558, 116639. <http://dx.doi.org/10.1016/j.desal.2023.116639>.
- Yang, Y., Zhao, R., Zhang, T., Zhao, K., Xiao, P., Ma, Y., Ajayan, P.M., Shi, G., Chen, Y., 2018. Graphene-based standalone solar energy converter for water desalination and purification. *ACS Nano* 12 (1), 829–835.

- Zeng, J., Wang, Q., Shi, Y., Liu, P., Chen, R., 2019. Osmotic pumping and salt rejection by polyelectrolyte hydrogel for continuous solar desalination. *Adv. Energy Mater.* 9 (38), 1900552. <http://dx.doi.org/10.1002/aenm.201900552>.
- Zhang, Y., Xiong, T., Nandakumar, D.K., Tan, S.C., 2020. Structure architecting for salt-rejecting solar interfacial desalination to achieve high-performance evaporation with in situ energy generation. *Adv. Sci.* 7 (9), 1903478.
- Zhang, Q., Yi, G., Fu, Z., Yu, H., Chen, S., Quan, X., 2019. Vertically aligned janus mxene-based aerogels for solar desalination with high efficiency and salt resistance. *ACS Nano* 13 (11), 13196–13207.
- Zhang, Z., Zhang, H., Zhang, Q., Ye, Y., Zheng, Y., Zuo, X., Yang, Q., Tang, H., Jin, S., Li, G., 2024. Highly salt-resistant 3d melamine sponge-polypyrrole composites for efficient solar interfacial evaporation. *React. Funct. Polym.* 198, 105883.
- Zupin, Željko, Štampfl, V., Kočevar, T.N., Tomc, H.G., 2024. Comparison of measured and calculated porosity parameters of woven fabrics to results obtained with image analysis. *Materials* 17 (4), 783. <http://dx.doi.org/10.3390/ma17040783>.